Biomedicine & Pharmacotherapy 195 (2026) 118996

Contents lists available at ScienceDirect

Biomedicine & Pharmacotherapy

journal homepage: www.elsevier.com/locate/biopha

New mitochondrial $K_V1.3$ conjugates are potent and specific inducers of apoptosis in cancer models

Špela Gubič [a,1], Marzia Fois [a,1], Xiaoyi Shi [b,1], Ivan Džajić [a], Daniela Secci [a], Katja Kološa [c], Alja Štern [c], Joshua A. Nasburg [d], Hai M. Nguyen [d], Veronica Carpanese [e], Gayathri Viswanathan [e], Vanessa Checchetto [e], Maša Omerzel [f,g], Tim Božič [f], Boštjan Markelc [f,h], Tanja Jesenko [f,i], Maja Čemažar [f,j], Ildiko Szabo [e], Heike Wulff [d], Bojana Žegura [c], Tina Kosjek [k], Andrej Emanuel Cotman [a], Tihomir Tomašič [a], Luis A. Pardo [b,*], Lucija Peterlin Mašič [a,*]

[a] University of Ljubljana, Faculty of Pharmacy, Aškerčeva cesta 7, Ljubljana 1000, Slovenia
[b] AG Oncophysiology, Max-Planck Institute for Multidisciplinary Sciences, Hermann-Rein-Str. 3, Göttingen 37075, Germany
[c] National institute of biology, Department of genetic toxicology and cancer biology, Večna pot 121, Ljubljana 1000, Slovenia
[d] University of California, Davis, Department of Pharmacology, 451 Health Science Drive, Davis, CA 95616, USA
[e] University of Padova, Department of Biology, Via U. Bassi, 58, Padova 35121, Italy
[f] Institute of Oncology Ljubljana, Department of Experimental Oncology, Zaloška 2, Ljubljana, Slovenia
[g] Faculty of Health Sciences, University of Ljubljana, Zdravstvena pot 5, Ljubljana 1000, Slovenia
[h] Biotechnical Faculty, University of Ljubljana, Jamnikarjeva ulica 101, Ljubljana 1000, Slovenia
[i] Faculty of Medicine, University of Ljubljana, Vrazov trg 2, Ljubljana 1000, Slovenia
[j] Faculty of Health Sciences, University of Primorska, Polje 42, Izola 6310, Slovenia
[k] Institut "Jožef Stefan", Jamova cesta 39, Ljubljana 1000, Slovenia

ARTICLE INFO

Keywords:
Mitochondrial targeting
Mitochondrial KV1.3
Apoptosis
Cancer

ABSTRACT

Mitochondrial $K_V1.3$ channels (mito$K_V1.3$) have emerged as promising targets for cancer therapy due to their role in regulating apoptosis, independent of upstream signalling pathways and Bcl-2 family protein levels. Here, we present a new non-psoralene $K_V1.3$ mitochondria-targeted conjugates. These conjugates, particularly *cis*-**8** and *cis*-**9**, exhibit nanomolar affinity and high selectivity for $K_V1.3$ while effectively inducing apoptosis in tumor cells. Unlike their parent $K_V1.3$ inhibitors, which lack cytotoxicity, the mito$K_V1.3$ conjugates induce rapid mitochondrial depolarization, and caspase-3/7 activation, culminating in dose-dependent tumor cell death in both 2D and 3D models. Mechanistically, *cis*-**8** and *cis*-**9** disrupt mitochondrial membrane potential and selectively target cancer cells, sparing normal cells at lower concentrations. Notably, $K_V1.3$ knockout models confirmed the dependence of cytotoxicity on mito$K_V1.3$ inhibition. The conjugates demonstrated robust antitumor activity in murine pancreatic intraepithelial neoplasia (PanIN)-derived organoids, with preferential action over normal pancreatic organoids, highlighting their tumor selectivity. Importantly, safety assessments showed no significant DNA damage or chromosomal aberrations at non-cytotoxic doses. This study introduces a new structural class of mitochondria-targeted $K_V1.3$ inhibitors with enhanced solubility compared to psoralen-based analogues. The unique mechanism of action, characterized by rapid depolarization and moderate ROS dependence, underscores their potential as selective anticancer agents. These findings warrant further investigation into *in vivo* efficacy and potential synergy with existing therapies.

* Corresponding authors.
E-mail addresses: tihomir.tomasic@ffa.uni-lj.si (T. Tomašič), pardo@mpinat.mpg.de (L.A. Pardo), lucija.peterlin@ffa.uni-lj.si (L.P. Mašič).
[1] equal contribution

https://doi.org/10.1016/j.biopha.2026.118996
Received 18 November 2025; Received in revised form 24 December 2025; Accepted 8 January 2026
Available online 15 January 2026

1. Introduction

Voltage-gated potassium channels (K_v) are transmembrane proteins that regulate the transport of potassium ions across the plasma membrane along their electrochemical gradient. [1,2] The K_v1 subfamily, also known as *Shaker* channels, consists of eight members ($K_v1.1$-$K_v1.8$). This study focuses on $K_v1.3$, which is found not only in the plasma membrane but also in the inner mitochondrial membrane (mito$K_v1.3$), [3] nuclear membrane, [4] and the membrane of the *cis*-Golgi apparatus. [5] Mito$K_v1.3$ was first identified in the inner mitochondrial membrane of lymphocytes, where it regulates the mitochondrial membrane potential and release of reactive oxygen species. [3] Both pharmacological and biophysical properties of mito$K_v1.3$ and plasma membrane $K_v1.3$ are indistinguishable, suggesting that they are encoded by the same gene [6] and exhibit similar pharmacology. $K_v1.3$ is imported into the inner mitochondrial membrane through the TIM23 machinery; [7] here, the much more negative mitochondrial membrane potential, despite similar potassium ion concentrations in the matrix and cytoplasm, drives potassium ions into the mitochondrial matrix, resulting in membrane depolarization through mito$K_v1.3$ activity. Conversely, inhibition of mito$K_v1.3$ leads to mitochondrial membrane hyperpolarization, [8] increased reactive oxygen species (ROS) production, and eventually apoptosis. Mito$K_v1.3$ function is also required to regulate matrix volume and ROS production. [9]

$K_v1.3$ channels are overexpressed in various primary cancers, as well as in cancer cell lines, [10] making them a potential tumor marker. [10–13] However, a clear pattern of altered $K_v1.3$ expression in cancer cells compared to healthy cells has not been established, partly due to the type and stage of the disease [14] and because expression studies often do not consider the channel's location. Despite this, $K_v1.3$ channels are overexpressed in breast, colon, prostate, pancreatic cancers, smooth and skeletal muscle cancers, and in mature neoplastic B cells in chronic lymphocytic leukemia. [15] With the exception of blood cancers, it is important to note that, because of high expression in immune cells, the overall presence of $K_V1.3$ in tumor samples does not necessarily reflect its abundance in tumor cells but can result from immune infiltration. *KCNA3* (the gene encoding $K_V1.3$) expression has been reported in a significant fraction of myeloma, lymphoma, and leukemia, as well as neuroblastoma, lung cancer, and sarcoma cell lines. However, it is also detected in specific lines from other tumor types. [16]

Mito$K_v1.3$ is involved in apoptosis signaling in cancer cells. [17] Inducing apoptosis in these cells by inhibiting mito$K_v1.3$ is an effective method for selectively killing them. [18] Proteins of the Bcl-2 family, such as Bcl-2-like protein 4 (Bax), inhibit mito$K_v1.3$, activating the intrinsic apoptotic pathway through membrane hyperpolarization, increased ROS production, and opening of the permeability transition pore (PTP), which releases cytochrome c and in turn leads to membrane depolarization. Membrane-permeable mitochondria-targeted $K_v1.3$ inhibitors can mimic this interaction by specifically inhibiting mito$K_v1.3$. Their selectivity for cancer cells over healthy cells is due to the high $K_v1.3$ expression and altered redox state in cancer cells, which are highly sensitive to ROS overproduction. [19] Thus, mito$K_v1.3$ inhibitors can promote cancer cell death while sparing healthy cells. [20,21]

Mitochondria, central to bioenergetic processes such as the Krebs cycle and ROS production, [22] have distinct features in cancer and normal cells, making them an oncological target. Selectively targeting ligands to mitochondria can reduce drug dosing and off-target effects, maximizing harm to cancer cells while minimizing damage to healthy cells. [23] The concept of selective mitochondrial targeting depends on the mitochondrial membrane potential, which is 3- to 5-fold larger (-180–220 mV versus approximately −60 mV in most cells) than that of the plasma membrane, causing positively charged molecules to accumulate in mitochondria to achieve electrochemical equilibrium. [24] Two strategies leverage these properties to deliver drugs to mitochondria: attaching a mitochondria-targeting ligand to the active compound or using nanocarriers to deliver drugs specifically to mitochondrial compartments. [25]

The specific mitochondria-targeting $K_v1.3$ inhibitors were developed on the basis of the first strategy, creating lipophilic, membrane-permeable conjugates of $K_v1.3$ channel inhibitors and mitochondria-targeting cations, like triphenylphosphonium (TPP^+). These inhibitors were designed by linking a TPP^+ moiety to a hydroxyl derivative of PAP-1 (PAPOH), a psoralen-based specific inhibitor of $K_v1.3$, [26] via stable alkyl (Fig. 1, PAPTP, **1**) or labile carbamate bonds (Fig. 1, PCARBTP, **2**). [21,27] PAP-1 alone was able to induce apoptosis only when applied together with inhibitors of the multidrug resistance pumps. [28] The mitochondriotropic psoralens PAPTP (**1**) and PCARBTP (**2**) were far more toxic to cancer cells than the parent PAP-1 *in vitro* and *in vivo*. Indeed, PAPTP and PCARBTP significantly decreased tumor volume *in vivo* in an orthotopic B16F10 mouse melanoma model. [21] In addition, the compounds achieved more than 90 % reduction in PDAC tumor volume when used concomitantly with gemcitabine and albumin-bound paclitaxel, [29] suggesting the possibility of synergy with other chemotherapeutic agents. [21,27] Treatment of mice with PCARBTP and PAPTP resulted in a significant reduction in human COLO 357 pancreatic tumors [27] and PAPTP very efficiently counteracted chronic lymphocytic leukemia in a genetic model of the disease. [30] A major limitation of psoralen-based $K_V1.3$ inhibitors like PAP-1 is their very low solubility in water (aqueous solubility < 1 mg/mL). [31] Psoralen-based mito$K_V1.3$ inhibitors further have short *in vivo* half-lives. In mouse blood, PCARBTP hydrolyzes completely within one hour to generate PAPOH. [21] Thus, new specific mito$K_V1.3$ inhibitors with suitable physicochemical properties for preclinical development are needed to overcome these drawbacks.

2. Results

2.1. Design of the first non-psoralene-based mito$K_V1.3$ conjugates

Initially, we tested the potential anticancer effects of our previously published parent $K_V1.3$ inhibitors *trans*-**3** (*N*-(((1 *R*,4 *R*)-4-Hydroxy-1-(thiophen-2-yl)cyclohexyl)methyl)-2-methoxybenzamide), *cis*-**3** (*N*-(((1*S*,4*S*)-4-Hydroxy-1-(thiophen-2-yl)cyclohexyl)methyl)-2-methoxybenzamide), *trans*-**4** (*N*-(((1 *R*,4 *R*)-4-Hydroxy-1-(thiophen-3-yl)cyclohexyl)methyl)-2-methoxybenzamide) and *trans*-**5** (*N*-(((1 *R*,4 *R*)-4-Hydroxy-1-(phenyl)cyclohexyl)methyl)-2-methoxybenzamide), and *cis*-**5** (*N*-(((1*S*,4*S*)-4-Hydroxy-1-(phenyl)cyclohexyl)methyl)-2-methoxybenzamide) [32,33] on the pancreatic cancer cell line COLO 357, which expresses $K_V1.3$ and is sensitive to the cell-permeable $K_V1.3$ inhibitor clofazimine. [34] This cell line serves as an excellent model to compare the potencies of mitochondria-targeted $K_V1.3$ conjugates with parent $K_V1.3$ inhibitors. To justify the selection of the COLO-357 cell line for our experiments, we performed a comparative analysis of mitochondrial mass in three different cell lines: COLO-357, HeLa, and B16F10. Mitochondrial mass was assessed using flow cytometry and staining with nonyl acridine orange (NAO), a cardiolipin-binding dye that reflects mitochondrial membrane content independent of membrane potential. Among the tested cell lines, COLO-357 cells exhibited the highest mitochondrial content, supporting their relevance for studying mitochondria-targeting compounds (Fig. S1). As a non-tumor cell model, we used the telomerase-immortalized (and therefore non-transformed) hTERT-RPE1 cell line. The number of dead cells was quantified with the Cytotox green indicator of viability, represented as the number of dead cells (with fluorescent nuclei) normalized to the culture confluence using live cell imaging over a 24 h period (Fig. S2). 50 μM *trans*-**3**, *trans*-**4**, *trans*-**5**, and *cis*-**5** induced a modest but significant increase in cytotoxicity in non-tumor hTERT-RPE1 cells, while COLO 357 cells were insensitive to the parent $K_V1.3$ inhibitors (Fig. S2). We conclude that the cytotoxicity induced by the parent $K_V1.3$ inhibitors **3–5** is neither potent nor tumor-selective, most likely because these inhibitors cannot accumulate in mitochondria and bind to mito$K_V1.3$ ion channels in COLO 357 cells. Among all parent $K_V1.3$

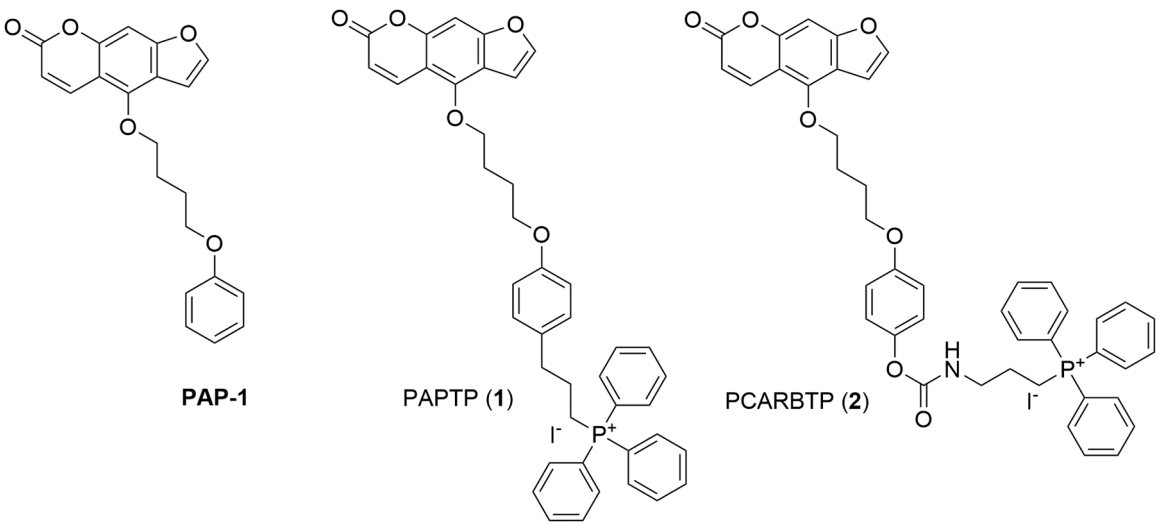

Fig. 1. $K_V1.3$ inhibitor PAP-1 and mitochondriotropic $K_V1.3$ conjugates PAPTP (**1**), PCARBTP (**2**). [21,28].

inhibitors, the most promising *cis*-**3**, was not cytotoxic to the non-tumor hTERT-RPE1 cells or the COLO 357 cancer cells. By attaching the TPP^+ MTM to *cis*-**3**, we obtained the most potent mitochondriotropic conjugates *cis*-**8** and *cis*-**9** of this series.

The design of new non-psoralen-based mito$K_v1.3$ inhibitors was guided by molecular docking calculations, revealing key interactions between the parent $K_v1.3$ inhibitors **3–5** (Scheme 1), [32,33] and the $K_v1.3$ channel pore. Docking studies showed that the *o*-methoxybenzamide and thiophene or phenyl moieties of inhibitors **3–5** were positioned below the selectivity filter, while the 4-hydroxycyclohexyl moiety was oriented towards the pore exit, as exemplified by inhibitor *trans*-**3** (Fig. 2A). Similar orientations were observed for the conjugate of *cis*-**3** with TPP^+ mitochondria-targeting moiety (MTM) via a propyl carbamate linker (compound *cis*-**8**), indicating space within the pore to accommodate larger substituents (Fig. 2C). Based on these insights, we synthesized a series of mito$K_v1.3$ conjugates (**6–11**) by attaching TPP^+ MTM to 4-benzamidomethyl-1-cyclohexanol-cored $K_v1.3$ inhibitors. The parent $K_v1.3$ inhibitors **3–5** were chosen for their inhibitory activity on $K_v1.3$ channels [33] and the presence of unsubstituted hydroxy group as an exit vector for the synthesis of conjugates. TPP^+, known for its effectiveness as a mitochondria-targeting moiety, [35–37] was attached to the inhibitors via three- and four-carbon carbamate linkers to create new mitochondriotropic $K_v1.3$ conjugates (Fig. 2B).

In contrast to the parent $K_V1.3$ inhibitors (**3–5**), the new mito$K_V1.3$ conjugates at 50 μM induced significant cytotoxicity in COLO 357 cells under standard culture conditions, resulting in a 4–12-fold increase compared to the control group treated with DMSO (the solvent of the compounds) (Fig. S3). Among the conjugates, *cis*-**8** (with a 3-carbon linker) and *cis*-**9** (with a 4–carbon linker), which are based on the 3-thiophenyl-substituted inhibitor *cis*-**3** (Scheme 1), demonstrated the

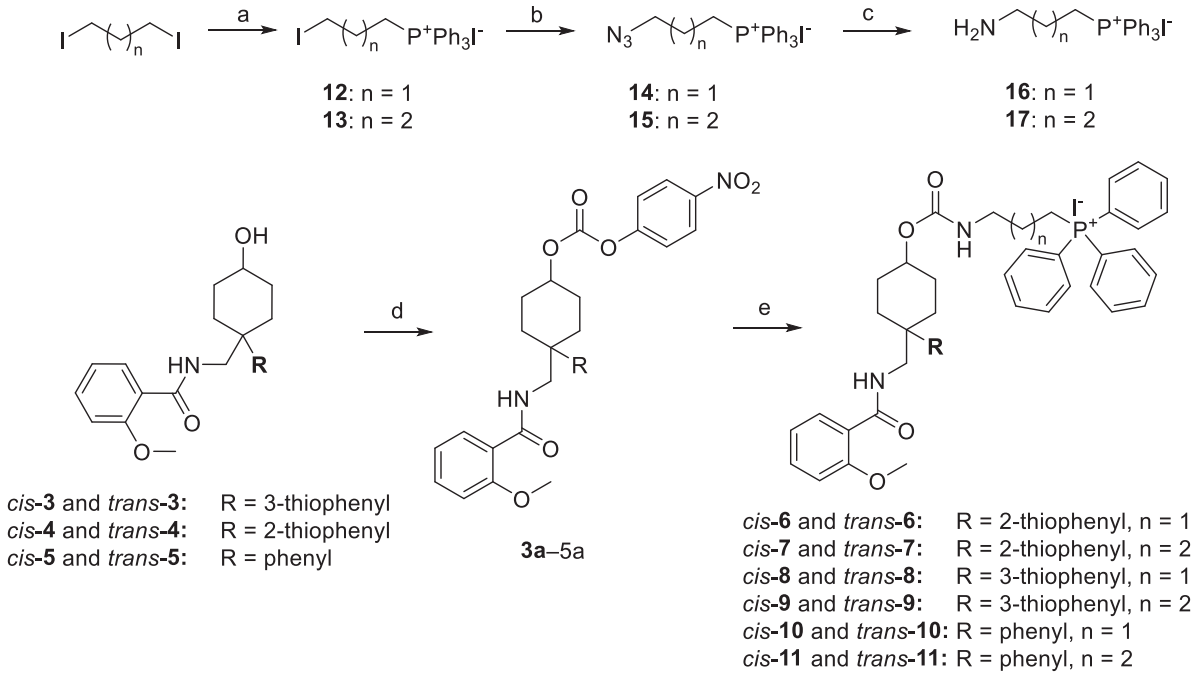

Scheme 1. Synthesis of new TPP^+-based $K_V1.3$ inhibitors with propyl or butyl carbamate linkers[a]. [a] Reagents and conditions: (a) toluene, 130 °C, 48 h (99 % yield); (b) NaN_3, ethanol, 70 °C, 24 h (96–99 % yield); (c) $H_{2(g)}$, Pd/C, methanol, rt, overnight (95–98 % yield); (d) 4-nitrophenyl chloroformate, Et_3N, DCM, rt, overnight; (e) **16** or **17**, DCM, rt, overnight (21–26 % yield).

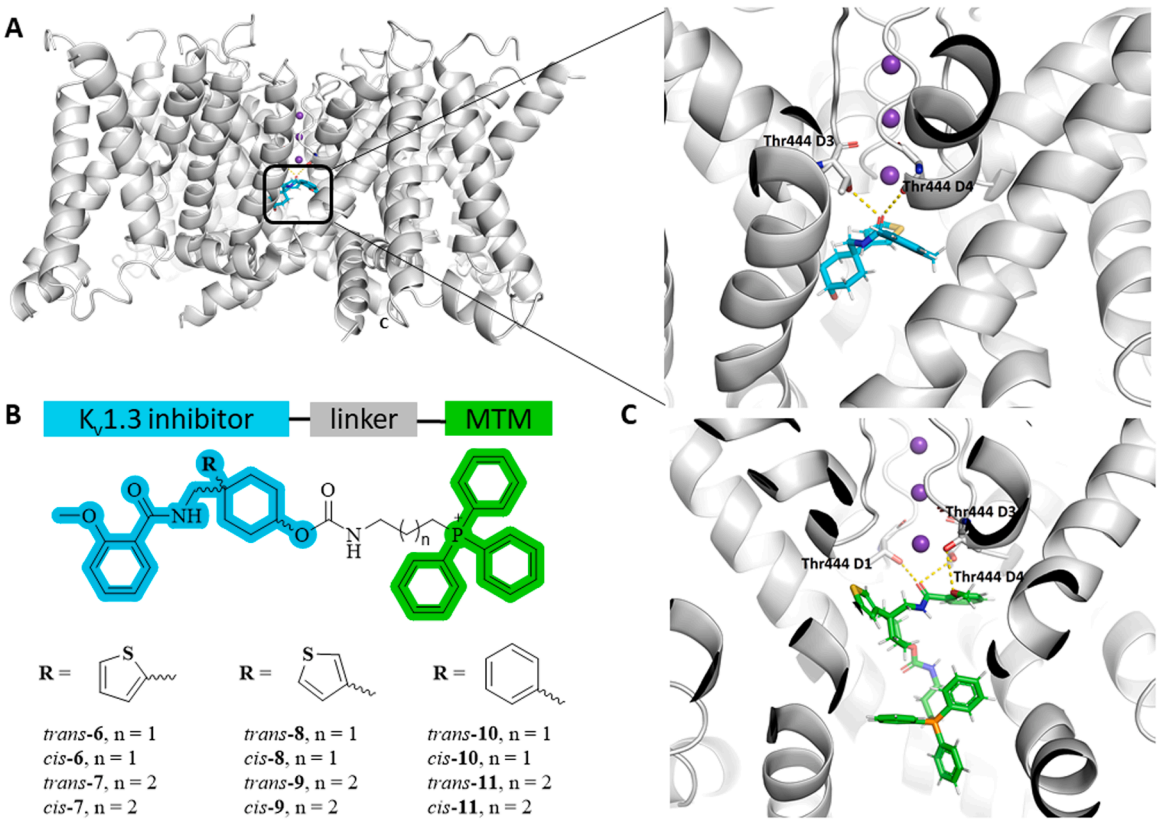

Fig. 2. A) Docking binding mode of inhibitor *trans*-3 (in cyan sticks) in the pore of K_V1.3 (in grey); B) Design strategy of mitoK_V1.3 inhibitors based on benzamide K_V1.3 inhibitors (in cyan) and triphenylphosphonium (TPP^+) (in green) as mitochondria-targeting moiety (MTM) connected by carbamate-bound alkyl linker (in black); C) Docking binding mode of the designed mitoK_V1.3 inhibitor *cis*-8 (in green) in the pore of the channel. For clarity, only residues forming hydrogen bonds with inhibitor are shown in grey sticks. Hydrogen bonds are shown as yellow dotted lines and potassium ions are presented as purple spheres.

highest potency, inducing a 13-fold increase in cytotoxicity. The other conjugates, which are based on the 2-thiophenyl- (conjugates **6** and **7**) and phenyl-substituted (conjugates **10** and **11**) inhibitors, were much less potent, indicating a structure-specific mitochondriotropic action. Additionally, the mitochondriotropic activity is stereoselective for conjugates **8** and **9**, where the *cis*-conjugates (*cis*-**8** and *cis*-**9**) were more potent than the *trans* isomers (*trans*-**8** and *trans*-**9**).

2.2. The mitoK_V1.3 conjugates cis-8 and cis-9 are potent K_V1.3 channels inhibitors

To confirm the inhibitory effects of the most potent mitochondrial conjugates on K_V1.3 currents, *cis*-**8** and *cis*-**9** were evaluated using whole-cell patch-clamp experiments on L929 fibroblasts stably expressing K_V1.3. The results showed that *cis*-**9**, with an IC_{50} of 373 nM, was more potent than *cis*-**8**, which had an IC_{50} of 535 nM for blocking K_V1.3 current. Both *cis*-**8** and *cis*-**9** were slightly less potent than their parent hydroxyl K_V1.3 inhibitor, *cis*-**3**, which had an IC_{50} of 226 nM under the same assay conditions (Fig. S4). Notably, all *cis* isomers were 7–10 times more potent than their corresponding *trans* isomers, indicating that the mitochondriotropic benzamide-based conjugates retain the stereoselective action of their parent K_V1.3 inhibitors (Table 1). This confirms the molecular modeling design, which suggested that there is sufficient space within the pore of the K_V1.3 channel to accommodate the TPP^+ MTM. The reference mitochondrial K_V1.3 conjugate, PAPTP (**1**), exhibited an IC_{50} value of 31 nM in CHO cells expressing K_V1.3. [25]

2.3. Cytotoxicity and selectivity of mitoK_V1.3 conjugates cis-8 and cis-9 on cancer and non-cancer cell lines

The most potent mitoK_V1.3 conjugates, *cis*-**8** or *cis*-**9**, were further tested on COLO 357 cells for dose dependence, as the EC_{50} determined to inhibit channel activity does not necessarily reflect the concentration that is required to exert an effect on intact cells. [38] Treatment with 50 μM of either *cis*-**8** or *cis*-**9** resulted in a faster onset of cytotoxicity compared to lower concentrations (5 μM and 25 μM; Fig. 3A and B). The overall cytotoxicity induction was similar for 25 μM and 50 μM, while 5 μM of *cis*-**8** or *cis*-**9** induced approximately half to two-thirds of the cytotoxicity observed with 25 μM or 50 μM treatments after 48 h (Fig. 3C and D).

Furthermore, we compared the selectivity of *cis*-**8** or *cis*-**9** on cancerous COLO 357 cells and normal hTERT-RPE1 cells at 1 μM or 2.5 μM. Cytotoxicity, determined by the total integrated intensity, showed moderate effects on COLO 357 cells, but not on hTERT-RPE1 cells already after 24 h. Conjugates *cis*-**8** and *cis*-**9** were nontoxic on non-tumor hTERT-RPE1 cells at 1 μM but effectively killed COLO 357 cells. At 2.5 μM, both cell types showed sensitivity; however, both *cis*-**8** or *cis*-**9** were more cytotoxic to COLO 357 cells (Fig. 3E and F).

Table 1
K_V1.3 inhibitions in whole-cell patch-clamp experiments on L929 fibroblasts.

Compound ID	K_V1.3 IC_{50} [nM]
cis-**3**	226 95 % CI = 212–238
trans-**3**	2180 95 % CI = 1830–2600
cis-**8**	536 95 % CI = 358–772
cis-**9**	369 95 % CI = 302–451

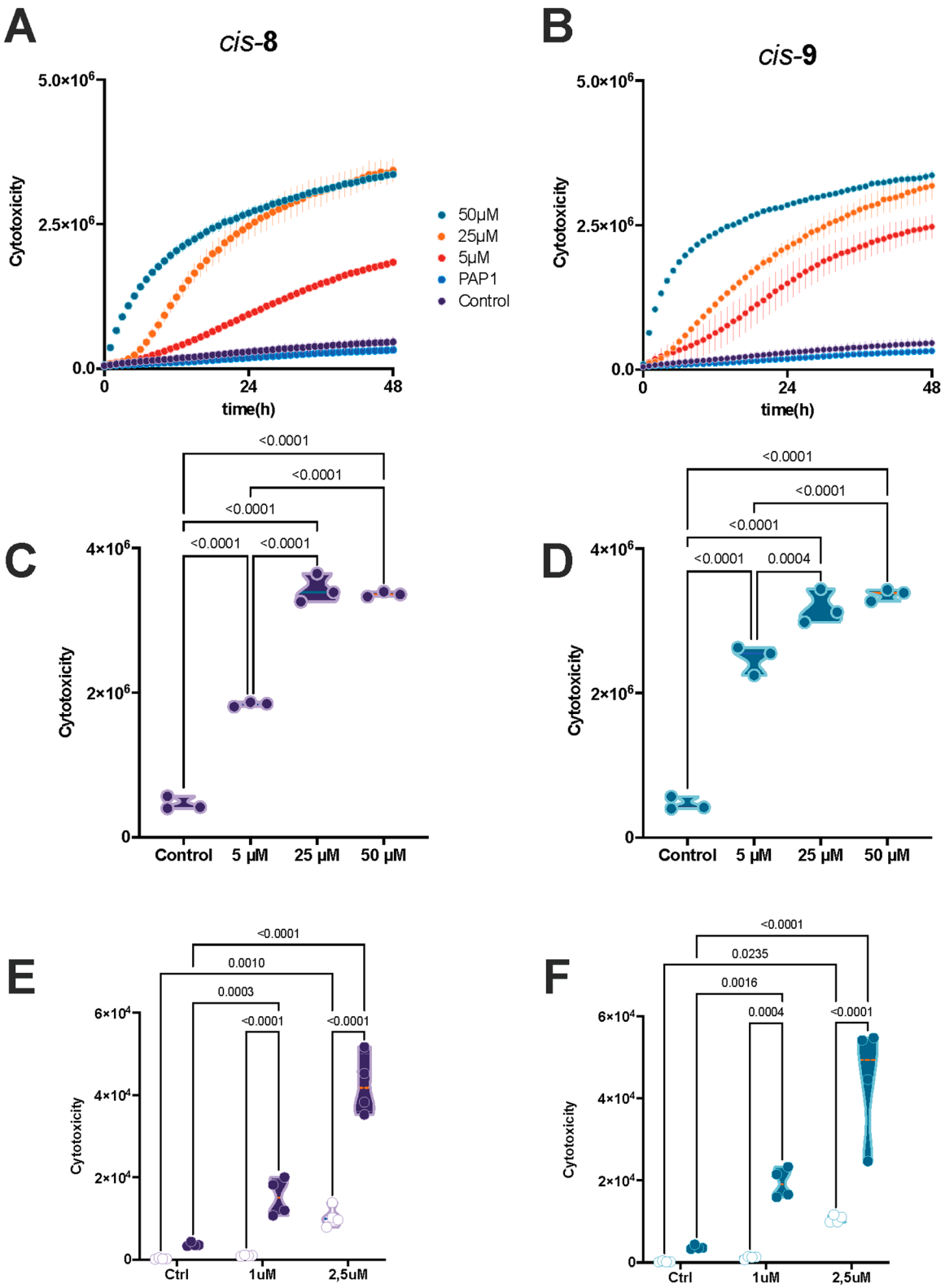

Fig. 3. A-D) Concentration dependence of cytotoxicity induced by mitoK_V1.3 inhibitors. COLO 357 cells were cultured in the presence of the fluorescent cytotoxicity reporter and the indicated concentration of the blocker for 48 h and the confluence of the culture and the fluorescence of the cytotoxicity indicator were monitored every hour in the presence of the indicated concentrations of *cis*-**8** (A) and *cis*-**9** (B). Mean ± standard deviation, N = 3. Statistical significance was determined by one-way ANOVA at the end of the 48 h period (C, D). E, F. *cis*-**8** (E) and *cis*-**9** (F) are nontoxic on non-tumor hTERT-RPE1 (open symbols) at 1 μM but produce the death of COLO 357 cells (solid symbols). At 2.5 μM, both cell types are sensitive, albeit to a different extent. The numbers indicate *p* values obtained by one-way ANOVA (N = 4).

Additionally, both conjugates had IC_{50} values in the micromolar range for the melanoma B16F10 cell line assayed with MTT test (Table S1) and demonstrated 3–6-fold selectivity against noncancerous cell lines C2C12 and L929 (Fig. S5).

2.4. Specificity of cis-8 and cis-9 action through $K_V1.3$ channels

We also performed an MTT assay to assess metabolic activity, which is linked to cell survival on B16F10 melanoma cells, which express $K_V1.3$ [28] and B16F10 cells with silenced expression of the channel. Both conjugates, *cis*-**8** and *cis*-**9**, efficiently reduced the viability of the cell line. The reduction in cell viability was significantly blunted in cells lacking $K_v1.3$ [9] when treated even with a high concentration (10 μM, which is approximately 5-fold higher of the EC_{50} value observed for B16F10 cells expressing $K_V1.3$) of *cis*-**8**, indicating the specificity of this compound in reducing cell viability through $K_V1.3$ (Fig. 4). The reduction of viability by *cis*-**9** showed a similar tendency but did not reach statistical significance at 10 μM. Data in Fig. 4 suggest that *cis*-**8** is more specific for $K_V1.3$ than *cis*-**9**; however, *cis*-**8** is less effective at reducing cell viability (Fig. 4) or inducing apoptosis (Fig. 8). Cell viability in this experiment was assessed using the MTT assay, which reflects the metabolic activity of cells rather than cell death per se. Therefore, we cannot exclude the possibility that *cis*-**9** causes a profound alteration of cellular metabolism. Consistent with this interpretation, *cis*-**9** did not induce cell death in MelanA cells at the same concentration.

2.5. Changes in mitochondrial inner membrane potential and release of ROS upon cis-8 and cis-9 treatment

Given the ability of both conjugates, *cis*-**8** and *cis*-**9**, to reduce mitochondrial metabolic activity, we investigated whether they, like PAPTP and PCARBTP, affect mitochondrial membrane potential using the membrane-potential sensitive dye, TMRM (tetramethylrhodamine methyl ester). As expected, both conjugates induced depolarization (see introduction), with *cis*-**9** being more efficient and comparable to the protonophore FCCP in triggering a rapid and complete loss of the membrane potential within an hour, already at a 1 μM concentration (Fig. 5A and B).

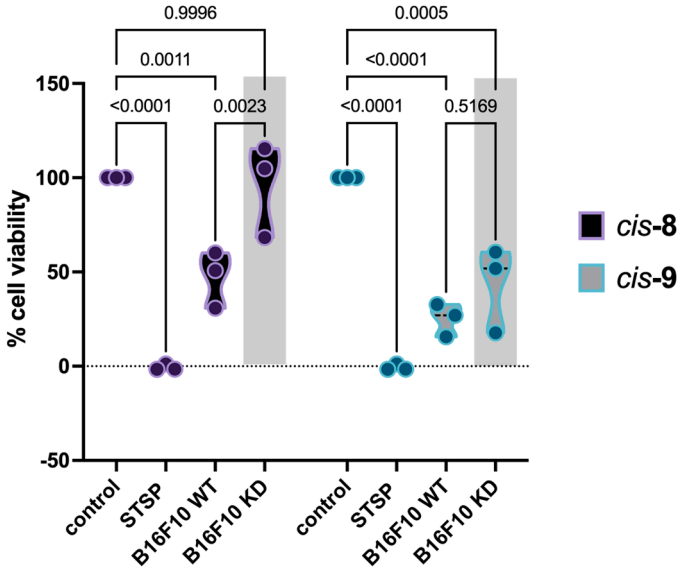

Fig. 4. MTT assay of B16F10 cells expressing or lacking $K_V1.3$. The effect of the compounds was significantly different for all concentrations (only 10 μM is depicted in the Figure; n = 3, ANOVA, $p < 0.05$), except for the cells without $K_V1.3$ treated with *cis*-**8**, whose viability was not significantly altered. Knockdown of $K_V1.3$ (shaded area) thus reduced the effect of the conjugates, but only significantly in the case of *cis*-**8**.

Next, we assessed the ability of the compounds to induce ROS release in real-time at the mitochondrial level using the MitoSOX assay (Fig. 5C and D). The ROS release of conjugates *cis*-**8** and *cis*-**9** was not significant and was much less pronounced compared to PAPTP and PCARBTP, likely due to the lack of the coumarin ring, which is proposed to interact with the Q module of complex I of the respiratory chain, thereby contributing to a strong ROS release. [39] We can conclude that mechanism of action of new benzamide-based mito$K_V1.3$ conjugates *cis*-**8** and *cis*-**9**, which lack a coumarin ring, differs from that of psoralene-based mito$K_V1.3$ conjugates, resulting in less pronounced ROS release.

In order to test whether the apoptosis induction in cancer cells is due to elevated ROS production, we tested the effect of a sublethal dose of 7-O-(4-triphenylphosphoniumbutyl) quercetin iodide (Q-7BTPI), a mitochondriotropic quercetin derivative previously shown to enhance ROS release from mitochondria. [40] As expected, the anti-oxidant treatment (NAC+mitoTEMPO + PEG-SOD) reduced the Q7-induced ROS (Fig. 6). We have previously shown that application of anti-oxidants abolished both mitoKv1–3 channel blockage-related increased ROS production and apoptosis of cancer leukemic B cells (B-CLL). [41] On the other hand, a mild oxidative stress induced by applying a sub-lethal dose of Q-7BTPI significantly increased ROS production and caused apoptosis in normal human B lymphocytes upon an application of mitoKv1.3 channel blockers. [41] We reasoned that if the apoptosis induction by the new conjugates *cis*-**8** and *cis*-**9** was ROS production-dependent, they would behave such as leukemic B-cells upon an application of anti-oxidants. If the apoptosis of cancer cells is ROS-independent, application of anti-oxidants would have no effect on the apoptosis induced by inhibition of mito$K_V1.3$ channels by the new inhibitors. If the apoptosis of the compared normal cells was ROS production-independent, a mild oxidative stress induced by Q-7BTPI would not sensitize these cells to the pro-apoptotic activity of mito$K_V1.3$ channel inhibitors.

The same anti-oxidant mixture did not reduce drug-induced apoptosis in the B16F10 cells, strongly suggesting that the death is not mediated by ROS (Fig. 7). Q7 alone is not sufficient to induce death in MelanA, which are immortalized normal cells, and, importantly, *cis*-**8** and *cis*-**9** do not trigger apoptosis- neither alone, nor in combination with Q7, at least when applied at 10 or 15 μM concentrations (Fig. 7). Please note that the same concentrations instead induced apoptosis in B16F10 cells. These results indicate that *cis*-**8** and *cis*-**9** -induced apoptosis is not ROS-dependent and further confirm that *cis*-**8** and *cis*-**9** exert an apoptosis-inducing effect in cancer cells but not on healthy cells.

2.6. Apoptosis (Caspase-3/7 activation) induction by mito$K_V1.3$ conjugates cis-8 and cis-9 in 2D PDAC (COLO 357) Cells

The new mitochondriotropic conjugates *cis*-**8** and *cis*-**9** demonstrated cytotoxicity in several cellular models. Given the proposed mechanism of action (inhibition of mitochondrial $K_V1.3$), it is important to determine whether cell death occurs through apoptosis or another mechanism. Therefore, we measured activation of the effector caspases 3/7. In conventional 2D culture of COLO 357 cells, 25 μM of either *cis*-**8** or *cis*-**9** induced strong activation of caspases with similar potency (Fig. 8B and D). In contrast, they did not show a similar effect in non-tumor hTERT-RPE1 cells (Fig. 8A and C)).

2.7. Apoptosis (Caspase-3/7 Activation) induction and cytotoxicity by mitoKv1.3 conjugates cis-8 and cis-9 in 3D PDAC Cultured (spheroids) and pancreatic-derived organoids

We then tested the potency of mito$K_V1.3$ conjugates *cis*-**8** and *cis*-**9** on COLO 357 tumor spheroids, which represent a more realistic tumor model compared to 2D cell culturing, to determine the induction of cytotoxicity and apoptosis (Fig. 9). Both conjugates exhibited significant cytotoxicity induction 48 h after treatment, with a rapid onset observed

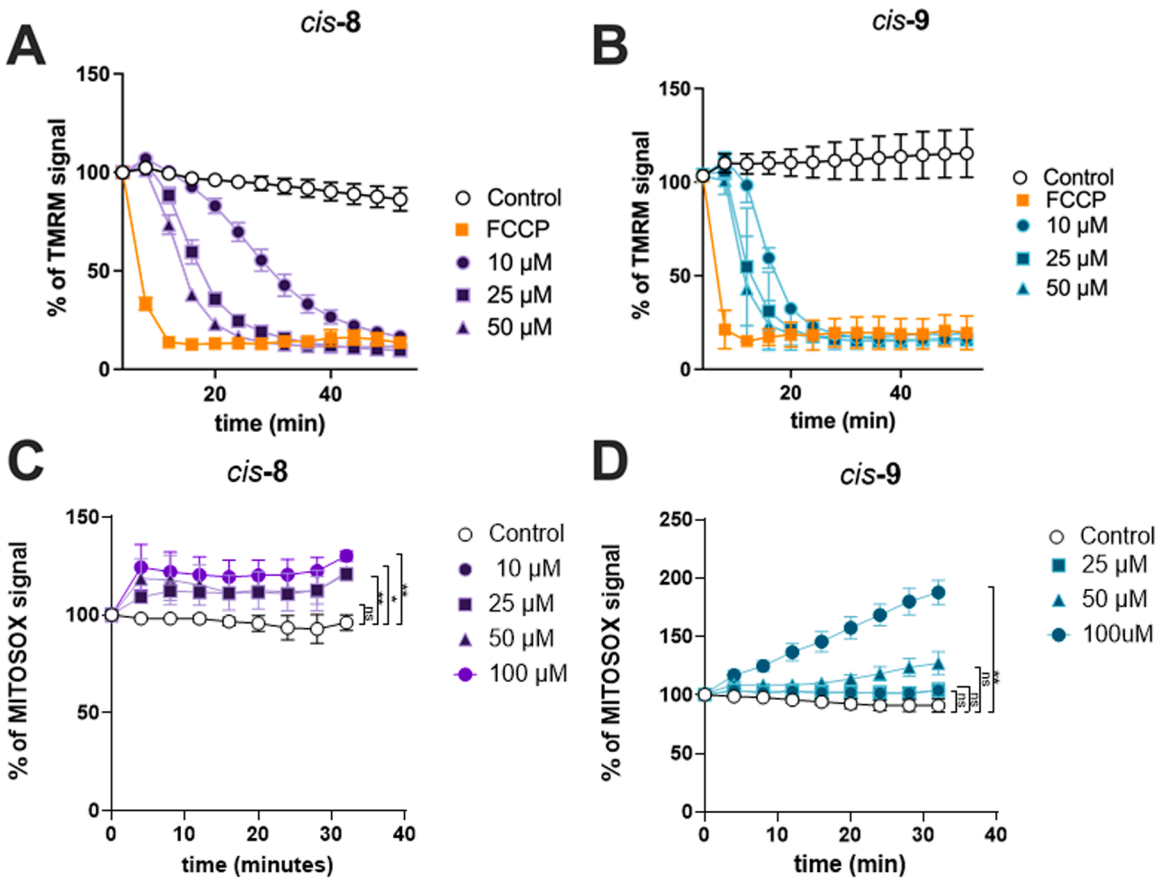

Fig. 5. Effects of *cis*-**8** and *cis*-**9** on mitochondrial function. A, B) *cis*-**8** and *cis*-**9** markedly depolarize the mitochondrial inner membrane. Measurements were performed and analyzed using Operetta HCS as described in the Materials and methods section. FCCP (1 μM) was used as positive control. Images were taken and analyzed at the indicated time points. The drugs were added at 0 time point on the graph (prior to this time point TMRM signal was recorded to ascertain stable signal (not shown). In 3 independent experiments for each drug, changes in membrane potential were statistically significant at all concentrations at the time point of 30 min. Mean values ± S.D. are shown (n = 3 different cultures). C, D) Mitochondrial ROS release of conjugates *cis*-**8** and *cis*-**9**. Measurements were performed and analyzed using Operetta HCS as described in the Materials and methods section. Images were taken and analysed at the indicated time points. Values are expressed as normalized mean values (with respect to the time point prior to the addition of the drugs, not shown) ± S.D. (n = 3 different cultures). 0 time point corresponds to the addition of the drugs. Statistically significant differences were achieved with the highest applied concentrations of both conjugates *cis*-**8** and *cis*-**9** only at 50 μM at 16 min.

as early as 12–14 h after addition of the *cis*-**8** and *cis*-**9** conjugates (Fig. 9A and C). The conjugates also demonstrated significant apoptosis induction, starting almost immediately after addition of the compounds, and peaking at 14 h (Fig. 9B and D). Caspase activity decreased from that time point, coinciding with the reduction in the number of viable cells. Both cytotoxicity and apoptosis assays showed a distinct induction of approximately 3–5-fold compared to the control solvent (DMSO) at their respective peak times (48 h for cytotoxicity and 14 h for apoptosis).

Compared with the treatments in conventional 2D cell culture (Fig. 3), apoptosis induction by *cis*-**8** and *cis*-**9** in spheroids exhibited a much faster onset and a more pronounced effect, but it declined within 24 h as the majority of cancer cells were destroyed by apoptosis. In 2D cell culture, the effect lasted longer (up to 48 h), likely reflecting the different growth behaviors.

We then studied the effects of *cis*-**8** and *cis*-**9** conjugates on a model less artificial than conventional or 3D culture, namely pancreatic organoids. We treated organoids derived from murine normal pancreas (mN) and from intraepithelial neoplasia (PanIN), the precursor or pancreatic carcinomas. We imaged the growth of both types of organoids in the presence of either conjugate or DMSO over a 72 h period. The area occupied by mN organoids in the images doubled in this period, while mP organoids almost tripled their density. The growth was slower in all cases in the presence of *cis*-**8** and *cis*-**9**; 10 μM of either compound abolished the growth of both types of organoids. However, at 1 μM and 5 μM concentrations, the compounds preferentially affected mP organoids. This effect was more evident for *cis*-**8**, as 5 μM *cis*-**9** intensely inhibited mN organoids. Nevertheless, mP organoids completely failed to grow in the presence of the mitoK_V1.3 conjugates (Fig. 10).

2.8. *In vitro genotoxicity assessment of cis-8 and cis-9*

To study the safety of both new conjugates, the potential genotoxicity of *cis*-**8** and *cis*-**9** was investigated *in vitro* in the human hepatocellular carcinoma cell line HepG2. The MTS (3-(4,5-dimethylthiazol-2-yl)-5-(3-carboxymethoxyphenyl)-2-(4-sulfophenyl)-2*H*-tetrazolium) assay was performed to evaluate the cytotoxicity of the tested compounds after 24 h of exposure and to determine non-cytotoxic concentrations for genotoxicity assays. Our results showed that both tested compounds were cytotoxic to HepG2 cells in the tested concentration range, with IC_{50} values of 35.3 ± 3.1 μM (*cis*-**8**) and 24.9 ± 1.3 μM (*cis*-**9**) after 24 h exposure (Fig. 11A). Concentrations in the range of IC_{70} (30.4 ± 3.1 μM (*cis*-**8**) and 22.3 ± 1.6 μM (*cis*-**9**)) were selected as the highest tested concentration for genotoxicity testing.

The potential genotoxic activity of *cis*-**8** and *cis*-**9** *in vitro* in HepG2 cells was evaluated using the comet assay, the cytokinesis block micronucleus (CBMN) assay, the γH2AX and pH3 assays and cell-cycle and proliferation analysis after 24 h exposure of HepG2 cells to the

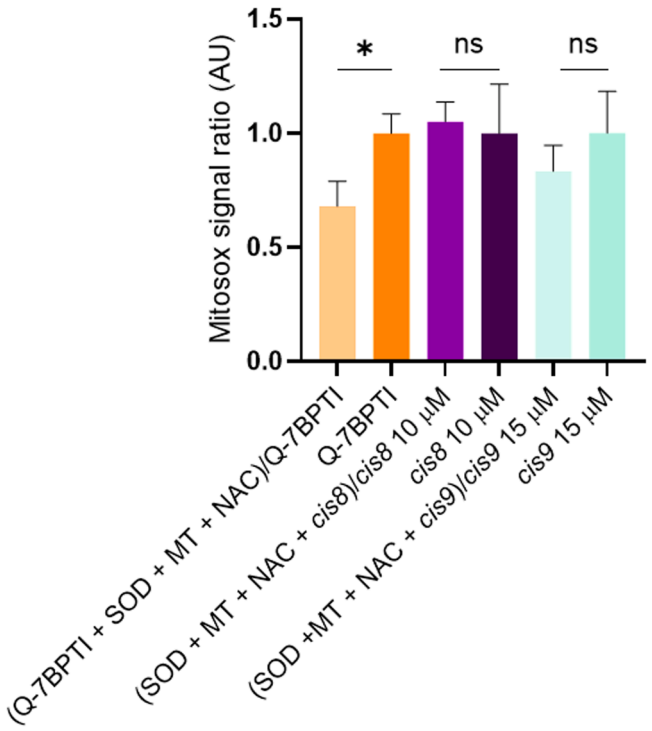

Fig. 6. Q-7BPTI induces ROS release in B16F10 cells which can be prevented by anti-oxidants. Concentrations: PEG-SOD (60 U) (indicated as SOD; MT (100 µM); NAC (5 mM); Q-7BPTI (0,5 µM). Cells were treated with Mitosox for 30 min and with *cis*-**8** and *cis*-**9** for 40 min and ROS production was assessed by FACS. N = 3 independent experiments, mean values +/- SEM are shown. ANOVA analysis, p-values are shown.

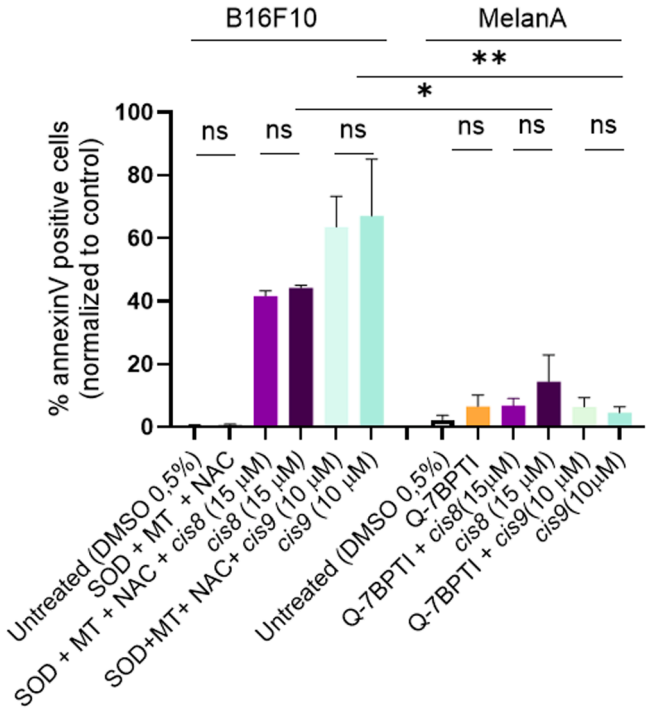

Fig. 7. Apoptosis does not depend on drug-induced ROS. Annexin-binding was assessed by FACS following treatment with the *cis*-**8** and *cis*-**9** for 16 h at the indicated concentrations in B16F10 and in Melan-A cells.

tested compounds. No significant induction of DNA damage was observed with the comet assay after the exposure to the tested compounds (Fig. 11B). Our results showed that *cis*-**8** and *cis*-**9** did not influence the genomic instability of HepG2 cells as no increase in the frequency of any of the evaluated types of chromosomal instability (CIN) biomarkers, including micronuclei (MNi), nuclear buds (NBUDs) and nucleoplasm bridges (NPBs), was observed (Fig. 11C). Furthermore, to determine the possible clastogenic and aneugenic effects of *cis*-**8** and *cis*-**9** compounds in HepG2 cells, phosphorylation of H2AX at Ser139, specifically induced by DNA double-strand breaks (DSBs), a marker of clastogenicity, and phosphorylation of histone 3 at serine 128 (pH3), a marker of aneugenicity, were examined (Fig. 11D). None of the compounds tested exerted aneugenic or clastogenic effects after 24 h exposure, except for *cis*-**9**, which slightly increased the amount of DNA double-strand breaks at the highest concentration (24 µM), which could have been the consequence of slight cytotoxicity observed at this concentration.

2.9. The effects of cis-8 and cis-9 compounds on cell cycle distribution and proliferation of HepG2

The effects of *cis*-**8** and *cis*-**9** compounds on cell cycle distribution and proliferation of HepG2 cells were investigated using flow cytometry. The results showed a significant change in cell cycle distribution, observed as a decrease in the percentage of cells in S phase and a concurrent increase in the percentage of cells in G2/M and/or G0/G1 phase, in cells exposed to *cis*-**8** at 30.5 µM and *cis*-**9** at 12, 18 and 24 µM. The reduction in cell proliferation was confirmed by a decrease in the number of Ki67-positive HepG2 cells at the same concentrations that influenced the cell cycle distribution, which is also in line with the results of the MTS assay.

2.10. Stability of conjugates cis-8 and cis-9 in PBS, plasma and cell matrix

To determine possible decay of conjugates *cis*-**8** and *cis*-**9** during the experiments, their stability was evaluated in phosphate-buffered saline (PBS), blood plasma and cell nutrient medium at two concentration levels. Spiked matrices were incubated with gentle shaking at 37 °C for 96 h (PBS, plasma) and for 24 h in the case of *in vitro* cell-based profiling experiments. The concentration of *cis*-**8** and *cis*-**9** was determined at the start (time 0) and after the incubation periods (96 h or 24 h) to assess any potential degradation of the two mitoK_V1.3 conjugates. The results showed no significant decay during the incubation periods, indicating that both conjugates are stable under the applied experimental conditions (Figure S8). The two most potent mitochondriotropic conjugates *cis*-**8** and *cis*-**9**, where the TPP^+-containing chain is linked to the benzamide core via a carbamic acid ester bond O-C(O)-N, were further investigated in kinetic experiments. After incubation in fresh human plasma at 37 °C, compounds *cis*-**8** and *cis*-**9** were quantitatively recovered unaltered after 24 h (Table S2), indicating that our new mitochondriotropic analogs are stable under physiological conditions.

2.11. Thermodynamic Solubility of cis-8 and cis-9 conjugates

The thermodynamic (TD) solubility of *cis*-**8** and *cis*-**9** was approximately 3-fold higher (Table 2) than the TD solubility of their parent hydroxyl K_V1.3 inhibitor *cis*-**3**, which was used for the synthesis of the two mitochondriotropic conjugates *cis*-**8** and *cis*-**9**.

3. Discussion

Mitochondrial potassium channels, particularly mitoK_V1.3, have emerged as promising targets for cancer therapy. Specifically, the direct modulation of mitochondrial inner membrane K_V1.3 channels, which triggers the intrinsic apoptosis pathway, is anticipated to facilitate the elimination of cancer cells. This process is independent of upstream

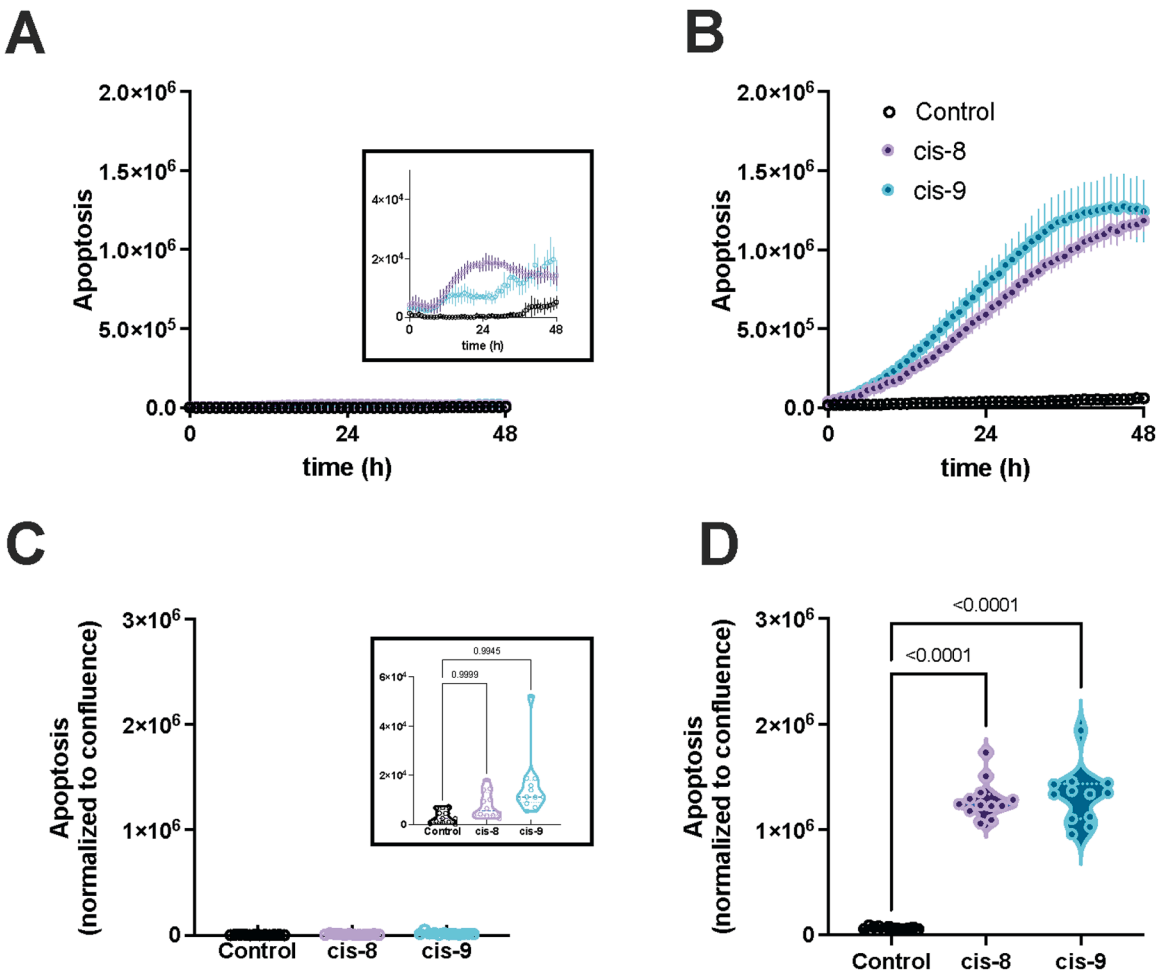

Fig. 8. Apoptosis induction by mitoK$_V$1.3 conjugates (25 μM) on non-tumor and tumor cells. Vehicle (DMSO) was also included as a control. A, B) Representative time course of the development of apoptosis over 48 h treatment expressed as total green object integrated intensity (GCU x μm^2/ image) in hTERT-RPE1 (A) and COLO-357 cells (B) by 25 μM of the indicated compound. The inset in A represents the same data presented with an expanded scale to show that there is a certain degree of apoptosis induction. Mean ± S.D., N = 4. C, D) Quantification of the apoptosis induction after 48 h treatment resulting from three biological replicates of the experiment depicted in A and B (n = 4 in each replicate) (C: hTERT-RPE1, D: COLO 357). The level of apoptosis is represented by the total integrated intensity (GCU x μm^2/Image) normalized to confluence (%). Ordinary one-way ANOVA test. The inset in D represents the same data presented with an expanded scale.

signalling pathways commonly altered in cancer patients (e.g., p53) and independent of the expression levels of pro- and anti-apoptotic members of the Bcl-2 family (e.g., Bax). [42] Apoptosis resistance is a prominent hallmark of cancer cells, often serving as a mechanism to evade drug-induced toxicity. Consequently, inhibitors targeting mitochondrial ion channels may prove beneficial for cells resistant to conventional chemotherapy. Extensive research on K$_V$1.3 pharmacology has provided a variety of potent and specific conjugates that can be targeted to the mitochondria using mitochondriotropic moieties like TPP$^+$. Psoralens, PCARBTP and PAPTP, which have a charged TPP$^+$ moiety bound to the specific psoralen-based K$_V$1.3 inhibitor PAP-1, specifically target mitoK$_V$1.3 and kill cancer cells *in vivo* through reactive oxygen species (ROS) mediated cell death. However, psoralen-based mitoK$_V$1.3 inhibitors have major drawbacks, such as extremely low solubility (less than 1 μM).

In this study, we introduced a series of thiophenyl- and phenyl-based K$_V$1.3 inhibitors with nanomolar affinity and high selectivity for K$_V$1.3. Molecular docking calculations indicated that the orientation of these inhibitors within the K$_V$1.3 channel pore allows enough space for accommodating a mitochondria-targeting moiety such as TPP$^+$. Consequently, we synthesized a series of new structural type of mitochondriotropic K$_V$1.3 conjugates with different K$_V$1.3 part and chain length to find better alternatives to psoralene based mitoK$_V$1.3 conjugates with better properties. Although the parent K$_V$1.3 inhibitors were not cytotoxic to tumor cells (Fig. S2), the presence of an MTM conferred cytotoxicity (Fig. S3). Among the new conjugates, *cis*-**8** and *cis*-**9** stood out as the most potent, with the *cis* isomers exhibiting the highest potency. These conjugates retained their ability to block K$_V$1.3 currents, as demonstrated in electrophysiological studies on K$_V$1.3 heterologously expressed in L929 fibroblasts, with only a slight increase in IC$_{50}$ values compared to parent K$_V$1.3 inhibitors. Importantly, the *cis* isomers were consistently more potent than the *trans* ones, correlating with the observed cytotoxicity and indicating a link between K$_V$1.3 current inhibition and cytotoxicity.

The cytotoxic effects of these new conjugates *cis*-**8** and *cis*-**9** were dose-dependent and preferentially targeted tumor cells. Murine melanoma B16F10 cells were the most sensitive to *cis*-**8** and *cis*-**9**, followed by rapidly dividing mouse myoblasts C2C12, and murine fibroblasts L929, indicating a preference for killing tumor cells over non-cancerous cells at least at a given concentration range. Human pancreatic cancer cells COLO 357 also exhibited dose-dependent cell death in response to these conjugates. Notably, the telomerase-immortalized human epithelial cell line hTERT-RPE1 was unaffected at lower concentrations, further underscoring the selectivity of the conjugates *cis*-**8** and *cis*-**9**. The requirement of K$_V$1.3 presence for inducing cell death was confirmed by reduced sensitivity in K$_V$1.3 knockout B16F10 cells.

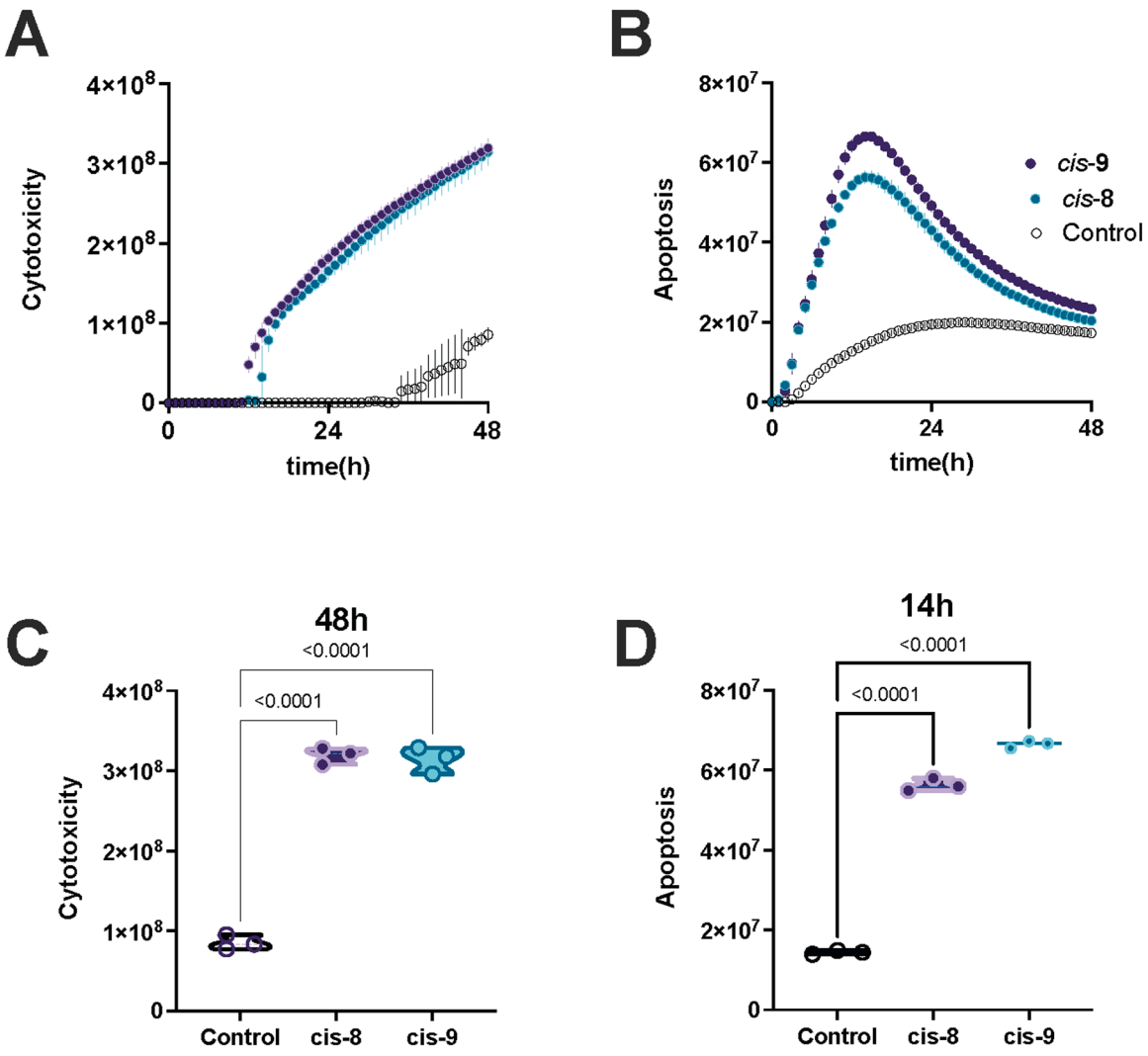

Fig. 9. Cytotoxicity and apoptosis induction by mitoK_V1.3 inhibitors (25 μM) on PDAC spheroids. Black: control (DMSO); Purple, *cis*-**8**. Green: *cis*-**9**. A, B) Representative data for the time course over 48 h of the induction of cytotoxicity (A) and apoptosis (B). Both were determined by the total integrated fluorescence intensity (GCU x μm^2/Image) of the corresponding reporter. Data are presented as means ± SD. C, D) Effects 48 h after the start of treatment (cytotoxicity, C) or at the peak of apoptosis induction (apoptosis at 14 h, D) represented as total integrated intensity (GCU x μm^2/Image). Ordinary one-way ANOVA test from three independent experiments with at least three spheroids analyzed per condition.

Mechanistically, conjugates *cis*-**8** and *cis*-**9** disrupted mitochondrial function by inducing rapid depolarization of the inner membrane potential. Additionally, these conjugates increased ROS release, though to a much lesser extent than psoralen-based conjugates PAPTP and PCARBTP. This difference could be attributed to the absence of a coumarin ring, which directly interacts with complex I of the respiratory chain in PAP-1 derivatives. Since the equilibrium potential for K^+ is much less negative than $\Delta\Psi$, the effect of K^+ conductance is depolarizing; therefore, blocking an active K_V1.3 in the inner mitochondrial membrane would result in hyperpolarisation and increase of $\Delta\Psi$. The initial hyperpolarization can be a trigger for subsequent depolarization and apoptosis induction [42,43] and could be hidden in our experiments by the limited temporal resolution. The depolarization observed is relatively fast, and faster than reported for the psoralen-based conjugates. Combined with the more modest increase of ROS levels, it is plausible that although both groups of compounds block mitoK_V1.3, the precise mechanism differs, allowing the prediction of different target cell populations depending on their dependence on ROS and oxidative phosphorylation.

Apoptosis, a key mechanism for the anticancer effects of these conjugates, was confirmed through caspase-3/7 activation in both 2D and 3D cell cultures. Caspase 3/7 activation in COLO 357 cells occurred rapidly upon addition of the conjugates, whereas the effect was negligible in hTERT-RPE1 cells, indicating selectivity for tumor cells. The rapid onset of apoptosis and subsequent cell death in COLO 357 spheroids highlighted the potential of these conjugates *cis*-**8** and *cis*-**9** in more complex tumor models. Additionally, the efficacy of conjugates *cis*-**8** and *cis*-**9** was validated in murine organoids derived from normal pancreas and pancreatic intraepithelial neoplasia (PanIN). Although both types of organoids were sensitive to the conjugates, the effects were qualitatively and quantitatively more intense on PanIN organoids, indicating their preferential action on malignant cells.

Safety assessments in HepG2 cells demonstrated that conjugates *cis*-**8** and *cis*-**9**, at non-cytotoxic concentrations, did not induce significant DNA damage or chromosomal aberrations. Cell cycle analysis revealed a significant reduction in S phase and an increase in G2/M phase, correlating with decreased proliferation in response to these conjugates.

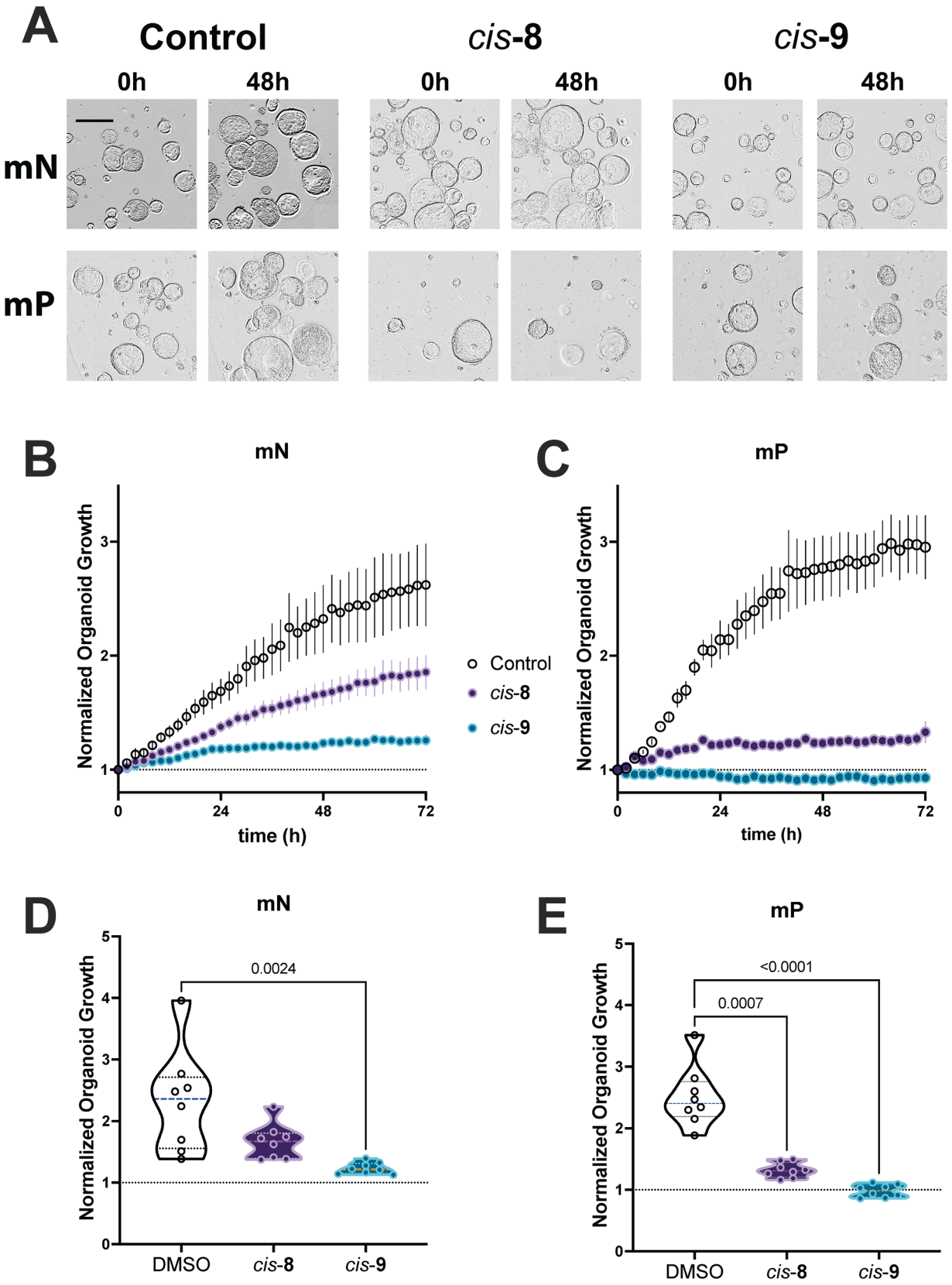

Fig. 10. Conjugates *cis*-**8** and *cis*-**9** inhibit the growth of murine pancreatic organoids. A) Representative images of organoid cultures taken at time 0 and after 48 h of treatment with the indicated conjugates. The upper row corresponds to mN organoids. Note that treated organoids in mP appear darker and with an inhomogeneous surface, indicating loss of viability. Scale bar: 500 μm. B, C) Growth curves of organoids in the presence of 5 μM *cis*-**8** and *cis*-**9** show the inhibition of growth for both types of organoids, although the effect was more intense for mP. The area occupied by organoids was normalized to the start of treatment. Mean ± SEM for three biological replicates with four technical replicates each. D, E) Comparison of the growth of organoids after 48 h treatment with 5 μM of the indicated conjugates (One-way ANOVA with Dunnett's test).

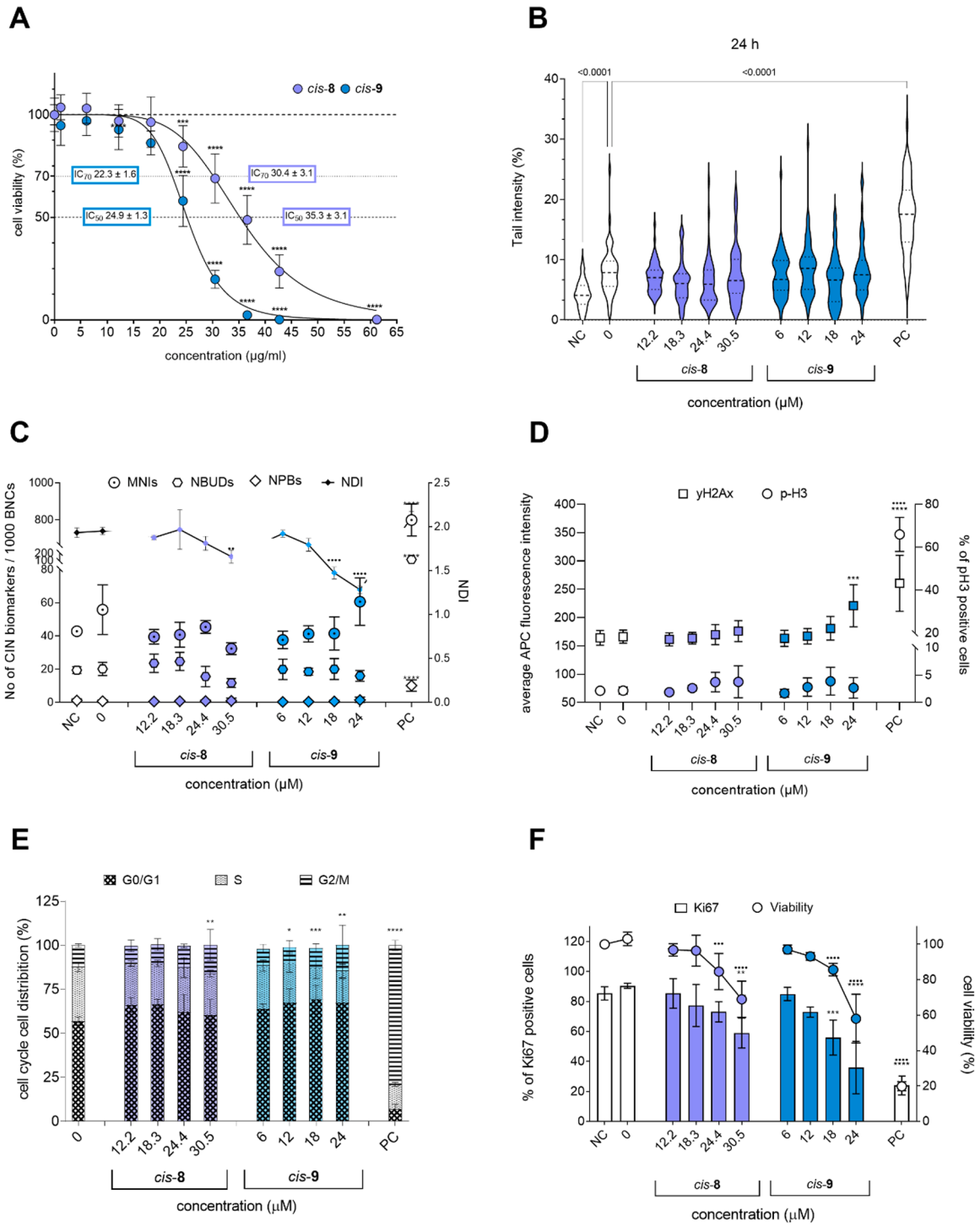

Fig. 11. Genotoxic activity of the compounds *cis*-**8** and *cis*-**9** in HepG2 cells. A) Effects of *cis*-**8** and *cis*-**9** on cell viability (MTS assay) are expressed as the percentage of the solvent control (0; 0.5 % DMSO — upper dashed line). 5 % DMSO was used as the positive control (PC) and reduced cell viability by 25.6 ± 4.7 % (data not shown). The dashed line in the middle represents the threshold of 70 % viability and the lower dashed line represents 50 % viability. IC_{50} and IC_{70} values are shown. B) Induction of DNA damage by *cis*-**8** and *cis*-**9**, detected with the comet assay. Data are expressed as violin plots with 95 % confidence interval. PC: 30 μg/mL BaP. C) Induction of chromosomal instability (CIN) biomarkers in HepG2 cells after 24 h of exposure to *cis*-**8** and *cis*-**9**. The frequency of micronuclei (MNi), nucleoplasmic bridges (NPBs) and nuclear buds (NBUDs) per 1000 binucleated cells (BNCs), and the nuclear division index (NDI) are shown. PC: 0.5 μg/mL etoposide. D) Characterization of aneugenic/clastogenic effects after 24 h of exposure to *cis*-**8** and *cis*-**9** compounds. The distribution of mean γH2AX APC fluorescence intensity and pH3 positive cells are presented. Etoposide (0.6 μg/mL) and colchicine (0.004 μg/mL) served as PC, respectively. E) The distribution of cells in the cell cycle phases was determined by flow cytometric analysis with Hoechst 33342 staining. Data are presented as percentages of cells in the G0/G1, S and G2/M phases. PC: Etoposide 0.6 μg/mL. F) Percentage of Ki67 positive cells determined by flow cytometry. Results are presented as mean ± SD (N = 3). Cell viability at the corresponding concentrations PC: Etoposide 0.6 μg/mL. In all tests NC is the negative control (growth medium), 0 is the solvent control (0.5 % DMSO). Asterisks (*) indicate a statistically significant difference between the samples and the SC: * $p \leq 0.05$, ** $p \leq 0.01$, *** $p \leq 0.001$, **** $p \leq 0.0001$.

Table 2
Thermodynamic (TD) solubilities for tested compounds.

Compound ID	TD solubility [μM]
cis-**3**	72
cis-**8**	233
cis-**9**	186

4. Materials and methods

4.1. Molecular docking

Molecular docking calculations were performed using Schrödinger Release 2023–1 (Schrödinger, LLC, New York, NY, USA, 2023). The cryoEM structure of $K_v1.3$ (PDB entry: 7SSV) with Fab-ShK fusion [44] was prepared using Protein Preparation Wizard with the default settings: bond orders were assigned using CCD database, missing hydrogens were added, termini were capped, the missing side chains were modelled with Prime, and het protonation states (pH 7.0 ± 2.0) were modelled with Epik. [45] The receptor grid was calculated for the ligand binding site, which was centred on the pore of channel (grid center 135.56, 136.89, 130.18). Ligand structures were prepared using LigPrep module and ionized with Epik at pH = 7.4 using OPLS4 force field. The compounds were then docked using the Glide XP protocol as implemented in Schrödinger Release 2023–1 (Glide, Schrödinger, LLC, New York, NY, USA, 2023). The highest scored docking conformation was used for analysis and presentation.

4.2. The synthesis of Mito$K_V1.3$ conjugates

The synthesis of conjugates **6–11** is detailed in Scheme 1. The α,ω-diiodoalkanes (Scheme 1) were refluxed with triphenylphosphine in toluene to produce the corresponding iodoakyltriphenylphosphonium iodides **12** and **13**. These intermediates were then converted to the azides **14** and **15** through nucleophilic substitution in ethanol and finally reduced by catalytic hydrogenation to yield the corresponding amines **16** and **17**. Compounds *trans*-**3**, *cis*-**3**, *cis*-**4**, *trans*-**4**, *trans*-**5**, and *cis*-**5** were prepared as previously described [32,33] and used to synthesize new mito$K_v1.3$-targeting conjugates with propyl carbamate or butyl carbamate linkers (Scheme 1). Thus, the cyclohexanols *cis*-**3**, *trans*-**3**, *cis*-**4**, *trans*-**4**, *cis*-**5** and *trans*-**5** were reacted with 4-nitrophenyl chloroformate to form 4-nitrophenyl carbonates **3a**–**5a**, which were then reacted with amines **16** and **17** to yield the conjugates **6–11**. Detailed experimental procedures for chemistry are presented in Supporting information (*Chemistry*).

4.3. Cell lines

All the cell lines used in this study (Table 3) were maintained in a humidified atmosphere at 5 % CO_2 and 37 °C. The cells were periodically tested for mycoplasma infection following the protocols of the participating laboratories.

4.4. Electrophysiology

Mouse L929 fibroblasts stably expressing mouse $K_V1.3$ were generated in 1994 and cultured as previously described. [46] All experiments were conducted with an EPC-10 amplifier (HEKA, Lambrecht/Pfalz, Germany) in the whole-cell configuration with a holding potential of −80 mV. Pipette resistances averaged around 2.5 MΩ. Compound solutions were prepared fresh daily in Na^+ Ringer from 10 mM stock solutions in DMSO. For current measurements, we used an internal pipette solution containing 160 mM KF, 2 mM $MgCl_2$, 10 mM HEPES, and 10 mM EGTA, with a pH of 7.2 and an osmolarity of ~ 300 mOsm. Sodium Ringer was used as an external solution containing the following: 160 mM NaCl, 4.5 mM KCl, 2 mM $CaCl_2$, 1 mM $MgCl_2$, and 10 mM HEPES, with a pH of 7.4 and an osmolarity of ~ 300 mOsm. Currents were elicited with a 200-ms voltage step to + 40 mV, followed by 45 s of holding at a resting membrane potential of −80 mV. A use-dependence protocol, whereby cells were pulsed to 40 mV every 1 s, was used prior to the step protocol for the compound to ensure that channel kinetics were as expected. If currents exceeded 2 nA 60–80 %, series resistance compensation was used. Concentration-dependent current inhibition, measured as reduction of area under the current curve, was fitted with the Hill equation using GraphPad Prism 8 (GraphPad Software, La Jolla, CA). All data points represent at least 3 independent experiments and are presented as mean ± standard deviation (SD). IC_{50}s are reported with 95 % confidence intervals (CI).

Table 3
Details of the cell lines used in the study.

Cell line	Source	Medium	Additives
B16F10	ATCC	MEM DMEM	10 mM HEPES 10 % FBS 100 U/mL penicillin G 0.1 mg/mL streptomycin, 1 % non-essential amino acids
B16F10	ATCC	ADMEM	5 % FBS, 100 U/mL penicillin. 0.1 mg/mL streptomycin, 1 % GlutaMAX
C2C12	ATCC	ADMEM	5 % FBS 100 U/mL penicillin. 0.1 mg/mL streptomycin, 1 % GlutaMAX
COLO 357	pHioniC	RPMI-1640	10 % FBS 1 mM sodium pyruvate 1 mM HEPES
HepG2	ATCC	AMEM	5 % FBS 100 U/mL penicillin. 0.1 mg/mL streptomycin, 1 % GlutaMAX
L929	Merck Millipore	ADMEM	5 % FBS 100 U/mL penicillin. 0.1 mg/mL streptomycin, 1 % GlutaMAX
TERT-RPE1	ATCC	DMEM/F12	10 % FBS 10 μg/mL Hygromycin B
Melan-A	ATCC	RPMI-1640	10 % FBS, 100 U/mL penicillin G, 0.1 mg/mL streptomycin, 2 mM L-Glutamine and 200 nM phorbol 12-myristate 13-acetate (Sigma-Aldrich)

4.5. Cellular assays (viability, cytotoxicity and apoptosis)

Viability of B16F10, C2C12, and L929 cells was determined using the resazurin-based assay Presto Blue (Thermo Fisher Scientific). 500 B16F10 or C2C12, and 800 L929 cells were seeded onto 96-well plates (VWR) in 100 μL of Advanced Dulbecco's Modified Eagle Medium (ADMEM, Thermo Fisher Scientific) per well. After 24 h, compounds were diluted in DMSO to a stock concentration of 10 mM. For compounds *cis*-**8** and *cis*-**9** serial dilutions were prepared to reach the final concentration of 50, 35, 30, 25, 20, 15, 10, 5 and 1 μM in ADMEM containing 0.5 % DMSO. For all other compounds serial dilutions were prepared to reach the final concentration of 50, 25 and 10 μM in ADMEM. Immediately thereafter, 10 μL of each diluted compound was added to corresponding wells (1:10 dilution). After 72 h incubation, 10 μL of Presto Blue reagent (Thermo Fisher Scientific) was added to each well, followed by 1 h incubation in a humidified incubator at 5 % CO_2 and 37 °C. The fluorescence emission was measured with a multimodal microplate reader Cytation 1 (BioTek). The measured fluorescence intensity of the treated groups was normalized to the control, untreated group.

Alternatively, B16F10 cells cultured under the conditions detailed in Table 1 were assayed for growth/viability using MTT assays as previously described. [21,28] Briefly, cells were seeded (5–10 × 10^3 cells/-well) in standard 96-well plates and allowed to grow in medium (200 μL) for 24 h to ensure attachment. The growth medium was then replaced in the dark with a medium that contained the desired compound (from a stock solution in DMSO) at the final concentration. The final

concentration of DMSO was 0.1 % or lower in all cases (including controls). After incubation for 24 h, CellTiter 96 AQUEOUS One solution (Promega, Italy) was added to each well as indicated by the supplier. Absorbance was measured at 490 nm to detect formazan formation using a Packard Spectra Count or a Tecan Infinite 200 PRO plate reader.

In the case of hTERT-RPE1 and COLO 357 cells, growth was determined by high-content imaging using an Incucyte device (Sartorius). 10^4 cells/well were seeded in 96-well flat bottom culture plates and allowed to grow for 24 h. The compounds were then added dissolved in DMSO (that did not exceed 0.1 % final concentration, which was also added to the control) in the corresponding growth medium at the concentrations indicated in the Figures. Thereafter, images were taken every hour for several days. The phase contrast images were used to determine cell confluence using the mask generated with the Incucyte software which was trained with selected images. Cytotoxicity was determined using CytotoxGreen (Sartorius) following the supplier's recommendations. The reporter was added at the same time as the different treatments. Unless otherwise indicated in the Figure, cytotoxicity is reported as total green fluorescence integrated intensity per image divided by cell confluence and, when indicated, normalized to the value in the vehicle control (0.1 % DMSO).

Apoptosis in hTERT-RPE1 and COLO 357 cells was also determined in an Incucyte using the same protocol above, except that the green Caspase 3/7 reporter system (Sartorius) was added along with the test compounds. For apoptosis, images were acquired hourly for 24 h or 48 h (spheroids) after the addition of the compounds dissolved in DMSO (time 0) and the green caspase 3/7 activity reporter. Fluorescence intensity values were normalized against the apoptosis level observed in the presence of the solvent (DMSO). Symbols in the Figures denote biological replicates (each with three technical replicates).

Spheroids from COLO 357 cells were cultured in round bottom ultra-low attachment 96-well plates (Corning). The optimal seeding densities were empirically determined (8000 cells/well). The cells were suspended in 2 % Matrigel (Corning), centrifuged at 1000 × *g* for 10 min, and the spheroids were allowed to form in the incubator. Cell viability and apoptosis were determined by high-content imaging in an Incucyte live cell imaging device as above. As an apoptosis sensitizer, 8.9 μM cycloheximide was added to controls and treated spheroids. Symbols in the Figures denote biological replicates (each with three or four technical replicates).

MTT assay in B16F10 in the presence of $K_V1.3$ inhibitors with or without siRNA knockdown was evaluated by binding of fluorescein isothiocyanate (FITC)-labeled Annexin-V and FACS analysis. For downregulation of Kv1.3 expression by siRNA, we used a protocol previously described. [21,28] The sequences for the siRNA targeting human $K_v1.3$ were coupled to Alexa Fluo 555 (Hs_KCNA3_1 Flexi tube siRNA for $K_v1.3$ and All-star negative control siRNA as scramble/control; Qiagen). 80,000 adherent cells/well were seeded into a 12 well plate in 1 mL of the growth medium. After 24 h, the cells were transiently transfected with 2 μg siRNA/well using Lipofectamine 2000, as suggested by the supplier. After 48 h from transfection, cells were treated for 24 h with the various compounds as indicated.

4.6. Flow cytometry analysis of Annexin V

B16F10 or Melan-A cells were seeded in a 6-well plate and the following day were treated for 16 h as indicated in the figure legends. After the incubation, cells were harvested with trypsin/EDTA, washed twice with PBS, resuspended in 100 μL of annexin-binding buffer and stained with 2 μL of Annexin-V-APC conjugate for 15 min at room temperature. After staining, cells were diluted with an additional100 μL of Annexin-binding buffer and immediately analyzed by flow cytometry.

4.7. Organoid culture

To evaluate the toxicity on a more elaborate experimental model, the effects of the *cis*-**8** and *cis*-**9** conjugates were also tested on murine organoids, which were kindly shared by D. Tuveson's laboratory [47]. Unlike other 3D cultures, organoids result from the differentiation of stem cells and can recapitulate many of the genetic and functional features of the tissue from which they are derived. Normal pancreas (mN) and pancreatic intraepithelial neoplasia (PanIN, mP)-derived organoids were allowed to form in Matrigel domes. Once formed, the conjugates *cis*-**8** and *cis*-**9** were added to the medium and the domes were imaged every two hours in an Incucyte system. The area occupied by organoids was then determined for each image and used to estimate organoid growth. Organoids were grown in Matrigel domes in a medium based on Advanced DMEM:F12, with GlutaMax, Penicillin-streptomycin and 10 mM Hepes (all from Gibco/Thermo Scientific), and containing A 83–01 (3-(6-methyl-2-pyridinyl)-*N*-phenyl-4-(4-quinolinyl)-1*H*-pyrazole-1-carbothioamide, TGF-β inhibitor, TOCRIS, 0.5 μM), mouse EGF (Thermo Fisher, 50 ng/mL), human FGF-10 (Peprotech, 100 ng/mL), human GastrinI (TOCRIS, 10 nM), mouse Noggin (Peprotech, 100 ng/mL), *N*-acetylcysteine (Sigma, 1.25 mM), nicotinamide (Sigma, 10 mM), R-Spondin1 conditioned medium and B-27 supplement (Thermo-Fisher). The effect of compounds on the growth of organoids was analyzed using the phase contrast images in an Incucyte system and measured as the change in the fraction of surface occupied by organoids using the confluence determination masks of the Incucyte software.

4.8. TMRM fluorescence measurements using high-content microscopy

5000 cells/well of B16F10 WT cells were seeded and allowed to attach for 48 h in a 96-well plate. Following, the cells were treated with 20 nM of TMRM (tetramethylrhodamine methyl ester, Thermo-Fisher Scientific) and 2 μM of CSH (Sigma) dissolved in 50 μL of HBSS/well (10 mM HEPES buffered saline solution (HBSS—Hank's Buffered Salt Saline, Invitrogen, pH 7.4 with 1 g/L of glucose) and incubated at 37 ºC for 40 min. Subsequently, the cells were incubated with Hoechst dye (1:10000 dilution) for 20 min at 37 ºC. After incubation, medium was replaced with a fresh one containing 10 nM of TMRM and 2 μM of CSH. the same buffer was used during image acquisition. Alternate bright-field, Hoechst33,342 (Ex:360–400/Em:410–480 nm), and TMRM fluorescence (Ex:520–550/Em:560–630 nm) images were acquired sequentially, by using different magnification air objectives of the high-content screening (HCS) imaging system Operetta® and Harmony® 4.8 analysis software (PerkinElmer) [34]. After acquisition of basal fluorescence intensity, cells were treated with *cis*-**9** or *cis*-**8** or with FCCP. For analysis, the image segmentation was performed via detection of regions of interest (ROI; each ROI corresponds to a single cell) in the Hoechst 33, 342 channel. Background-corrected TMRM fluorescence intensity was then measured per each ROI and averaged [48].

4.9. Measurement of mitochondrial ROS release using high-content microscopy

5000 cells/100 μL/well of B16F10 WT cells were seeded and allowed to be attached for 48 h and then the cells were treated with 2 μM of MitoSOX and incubated at 37 ºC for 30 min. Subsequently, the cells were incubated with Hoechst 33,342 dye (1:10000 dilution) for 20 min at 37 ºC. After incubation, the medium was replaced with 50 μL of fresh HBSS/well and the analysis was performed as described in the previous version, using high-content screening (HCS) imaging system Operetta® and Harmony® 4.8 analysis software.

4.10. Flow cytometry analysis of ROS production

B16F10 or Melan-A cells were seeded in a 6-well plate and the day after cells were pre-treated for 2 h with SOD-PEG (60 U/mL), NAC (300 mM), MitoTEMPO (100 μM) and then treated with different compounds (as indicated in the figure legend). After the treatment, cells were harvested with trypsin/EDTA, washed twice with PBS and stained

with 5 μM Mitosox, 2 μM Cyclosporin H in HBSS for 30 min at 37°C. After staining, cells were washed, resuspended in 200 μL of HBSS, and immediately analyzed by flow cytometry.

4.11. Cytotoxic and genotoxic activity of selected compounds in the HepG2 cell line

The HepG2 cell line (ATCC-HB-8065™) was used as model system for the *in vitro* genotoxicity assessment of *cis*-**8** and *cis*-**9**. Non-cytotoxic concentrations for the assessment of genotoxic activity of compounds studied were determined using the tetrazolium-based (MTS) assay (Cell Titer 96 AQueous Non-Radioactive Cell Proliferation Assay; Promega, Madison, WI, USA). Cells were seeded on 96-well microtiter plates (Nunc, Thermo Fisher Scientific, Waltham, MA) at a density of 10.000 cells/well for 4 h and 8.000 cells/well for 24 h of exposure and left to attach overnight. The next day, the culture medium was replaced with fresh medium containing graded concentrations (from 0.5 to 100 μM) of *cis*-**8** or *cis*-**9**. A negative control (cell culture medium), a vehicle control (0.5 % DMSO), and positive controls (7 and 5 % DMSO for 4 and 24 h of exposure, respectively) were included in the experiments. After exposure, 40 μL of the (20:1), MTS /PMS mixture was added to each well containing 200 μL medium. After 3 h of incubation (37 °C, 5 % CO_2) the absorbance was measured at 490 nm using a spectrofluorometer Synergy MX (BioTek, Winooski, VT, USA). Cell viability is expressed as the percentage of solvent control (0; 0.5 % DMSO) at each exposure time point. Three biologically independent experiments were performed with five replicates per treatment time point. Statistical significance between the control and treated groups was determined by one-way analysis of variance and Dunnett's multiple comparison test using GraphPad Prism v9 (GraphPadSoftware, USA).

4.12. Comet assay

Potential induction of DNA damage following exposure of HepG2 cells to non-cytotoxic concentrations of *cis*-**8** and *cis*-**9** (2.5–25 μg/mL for 4 and 5–20 μg/mL for 24 h), was analysed with the alkaline comet assay, or single cell electrophoresis), according to the description by Žegura and Filipič [49], with minor modifications. Cells were seeded at a density of 80,000 cells/well on 12 well plates (Corning, Corning Costar Corporation, NY, USA). Cell nuclei were stained with GelRed according to the manufacturer's protocol. Images were acquired using a fluorescence microscope (Eclipse 800, Nikon, Tokyo, Japan) and analysed using the Comet IV software (Perceptive Instruments Ltd., Haverhill, UK). A negative control (cell culture medium), a vehicle control (0.5 % DMSO), and a positive control (benzo[*a*]pyrene, BaP, 30 μg/mL) were included in the experiments. Three independent experiments were performed, wherein fifty nuclei were analysed per experimental point. The Kruskal–Wallis nonparametric test and Dunn's multiple comparison test GraphPad Prism v9 (GraphPadSoftware, USA) were used to assess statistically significant differences in the percentage of tail DNA between the tested cell populations.

4.13. Cytokinesis block micronucleus assay (CBMN)

Potential induction of genomic aberrations following exposure of HepG2 cells to non-cytotoxic concentrations of *cis*-**8** and *cis*-**9** (5–20 μg/mL for 24 h), was analysed with the cytokinesis block micronucleus assay (CBMN). HepG2 cells were seeded on 25 cm^2 culture plates at a density of 700,000 cells/plate and allowed to adhere overnight. The next day, cells were exposed to graded non-cytotoxic concentrations of *cis*-**8** and *cis*-**9**. At the tested concentration none of the extracts decreased cell viability by more than 55 % as recommended by the OECD Test Guideline No. 487. [50] A negative control (cell culture medium), a vehicle control (0.5 % DMSO), and a positive control (etoposide, ET, 0.5 μg/mL) were included in the experiments. After the exposure, the cells were washed with 1 ×s PBS, medium containing cytochalasin B (2 μg/mL) was added, and the cells were incubated for an additional 26 h at 37 °C in 5 % CO_2 humidified atmosphere. The medium containing cytochalasin B was collected in a centrifuge tube, the cells were washed with PBS buffer, harvested, and added to the corresponding centrifuge tube. The slides were prepared as described by Štraser et al. [51] For the analysis, the slides were stained with Hoechst 33342 (1 μg/mL; Sigma, St. Louis MO, USA) and examined using the automated Matafer system (Metasystems). For each experimental point genomic aberrations (micronuclei (MNi), nuclear buds (NBUDs) and nucleoplasmic bridges (NBPs)) were counted in at least 1000 BNC. The NDI was estimated by scoring 500 cells with one to four nuclei and calculated using the formula [M1 + 2M2 + 3(M3 + M4)]/500, where M1, M2, M3, and M4 represent the number of cells with one to four nuclei, respectively. The experiments were repeated three times independently.

4.14. Determination of anti-proliferative and aneugenic/clastogenic effects of selected compounds using flow cytometry

HepG2 were seeded on 25 cm^2 culture plates at a density of 500,000 cells/plate and allowed to adhere overnight. The next day, cells were exposed to *cis*-**8** and *cis*-**9** compounds at concentrations of 10, 15, 20 and 25 μg/mL and 5, 10, 15 and 20 μg/mL for 24 h, respectively. Etoposide 0.6 μg/mL and colchicine 0.004 μg/mL (both obtained from Sigma, St. Louis MO, USA) were used as positive controls for the proliferation and γH2AX analysis, and p-H3 analysis, respectively. After 24 h of exposure, all cells were collected, washed twice in 1 × PBS and fixed in 75 % ethanol overnight at 4 °C for further labelling with anti-Ki67 antibody for cell proliferation analysis, Hoechst 33342 dye for cell cycle analysis, anti-H2AX pS139 antibody for DNA double strand break (DSB) analysis and anti-histone H3 pS128 antibody (all antibodies were obtained from Miltenyi Biotec, Germany) for analysis of aneugenic activity, as previously described. [52,53] Three biologically independent experiments were conducted and for each measured sample, 15,000 events were acquired with MACSQuant Analyzer 10 flow cytometer and MACSQuantify™ software (Miltenyi Biotech, Germany). For analysis of results, raw data were exported from MACSQuantify software and analysed with FlowJo V10 software (Becton Dickinson, New Jersey USA).

Statistically significant differences between the *cis*-**8** or *cis*-**9** exposed and control samples in the number of Ki67- and pH3-positive cells were determined by one-way ANOVA with Dunnett's multiple comparison test and statistically significant difference in the intensity of APC fluorescence signal (γH2AX) was determined by two-way ANOVA with Uncorrected Fisher's LSD using GraphPad Software v9. Cell cycle distribution was evaluated with the univariate Dean–Jett–Fox cell cycle model in FlowJo and statistical significance in the cell-cycle distributions was determined using the chi-square test in GraphPad. Statistical significance was defined as $p \leq 0.05$.

4.15. Quantitative chemical analysis applied in stability experiments

Cell medium: Two hundred microliters of the sample were put into 1.5 mL polypropylene microcentrifuge tubes. 250 μL of MilliQ water and 50 μL of the internal standard, *cis*-**8** or *cis*-**9** solution (50 μg/mL) were added and mixed well. The samples were extracted by 96-well plate solid phase extraction (SPE) using wide-polarity range Oasis HLB sorbent. After sorbent conditioning the samples were transferred to individual wells and were left to gravity-pass the sorbent. As follows, the sorbent was dried using a positive pressure-96 processor (Waters, Millford, MA, USA) at 15 psi nitrogen for 20 min. After elution with 1 mL of acetonitrile the extract was nitrogen-evaporated and reconstituted with 1 mL of MilliQ water and diluted 50-times.

Blood plasma: 100 μL of the plasma was put into 1.5 mL polypropylene microcentrifuge tubes. 80 μL of MilliQ water and 20 μL of the *cis*-**8** or *cis*-**9** solution (1 μg/mL) were added and mixed well. The mixture was vortexed and then transferred into Ostro™ 96-well plate

wells (Waters, Millford, MA, USA). Protein precipitation was achieved by the addition of 600 μL ice-cold acetonitrile with 1 % formic acid. In-well mixing was performed with vigorous pipette aspiration and subsequently pushed through the Ostro™ sorbent at 60 psi N_2 for 5 min using a positive pressure manifold. The eluates were blown down to 500 μL using nitrogen and finally filtered through 0.2 μm Phenex™ regenerated cellulose membrane syringe filters. (Phenomenex, Torrance, CA).

PBS: Five hundred microliters of PBS samples with low spike were mixed with 5 μL of *cis*-**8** or *cis*-**9** (1 μg/mL). PBS samples were additionally diluted, mixing 100 μL of each sample with 10 μL of *cis*-**8** or *cis*-**9** and 890 μL of PBS.

Instrumental analysis: For the instrumental analysis of *cis*-**8** or *cis*-**9**, an ultra-high-performance liquid chromatograph (UHPLC, Shimadzu, Kyoto, Japan) coupled to a hybrid quadrupole-linear ion trap mass spectrometry analyser QTRAP 4500 (Sciex, Framingham, MA, USA) with positive electrospray ionization (ESI+) was utilized. Ascentis Express C18 (5 cm × 2.1 mm, 2 μm) (Supelco, Bellefonte, PA, USA) column was used for separation. Separation was achieved using the gradient method and the following mobile phase composition: acetonitrile (mobile phase A) and 0.1 % formic acid in MilliQ water (mobile phase B). The gradient program started with 70 % B, remained so for 1 min, then decreased to 40 % B at 1.5 min and further to 20 % B at 5 min. It increased back to the initial 70 % B at 5.5 min where it remained for 2 min for column equilibration. The total mobile phase flow rate was 0.3 mL/min. An injection volume was 1.0 μL. The ion source parameters were maintained as follows: ion spray voltage + 4000 V; source temperature 600 °C; curtain gas (CUR) 35 psi; ion source gas 1 (GS1) 20 psi; ion source gas 2 (GS2) 30 psi. Each compound was monitored via a quantitative and two additional qualitative transitions in multiple reaction monitoring (MRM) mode.

4.16. Thermodynamic solubility

Thermodynamic solubility was determined as a concentration of a saturated solution in equilibrium (37 °C) in phosphate buffered saline (pH = 7.4) using HPLC method. For the phosphate-buffered saline (PBS), 2.38 g of disodium hydrogen phosphate dodecahydrate, 0.19 g of potassium dihydrogen phosphate, and 8.0 g of sodium chloride were added to distilled water (900 mL) and the solution was mixed overnight. The next day, it was diluted to 1000 mL with the same solvent and the pH was adjusted to 7.4. Samples (dry powders) were prepared by weighing the exact mass of compounds (about 1 mg) and then adding the appropriate volume of PBS to reach the final concentration of approx. 1 mg/mL. The samples were shaken (60 rpm) at 37 °C for 24 h using orbital shaking incubator. After 24 h they were centrifuged at 18000 rpm for 10 min. Samples for injection were prepared by diluting (1:2 or 1:10) the supernatant with a 1:1 mixture of 0.1 % TFA [v/v] in water and acetonitrile. For the 7-point calibration curves concentrated stock solutions of the compounds were prepared at concentrations of 10 mM and 0.5 mM in DMSO, which were diluted with a 1:1 mixture of 0.1 % TFA [v/v] in water and acetonitrile to a final concentration of 100 μM; 70 μM; 50 μM; 30 μM; 15 μM; 5 μM and 1 μM. Quality control (QC) samples were diluted from stock solutions with a 1:1 mixture of 0.1 % TFA [v/v] in water and acetonitrile to final concentrations of 60 μM, 20 μM, and 2 μM. Analytical reversed-phase UPLC analyses were performed using a modular system (Thermo Scientific Dionex UltiMate 3000 modular system; Thermo Fisher Scientific Inc., MA, USA).

Method: Waters Acquity UPLC® HSS C18 SB column (2.1 × 50 mm, 1.8 μm), T = 40 °C; injection volume = 5 μL; flow rate = 0.4 mL/min; detector λ = 290 nm; mobile phase A (0.1 % TFA [v/v] in water), mobile phase B (acetonitrile). Gradient: 0–2 min, 10 % B; 2–10 min, 10 %–90 % B; 10–12 min, 90 % B. Results are given in μM as an average value of two independent experiments. Results are given in μM as an average value of two independent experiments.

4.17. Statistical analysis

The number of independent experiments and the methods used to determine statistical significance are indicated in the corresponding figure legends. Statistical significance was in all cases defined as $p \leq 0.05$.

5. Conclusion

Our study highlights the potential of the newly synthesized benzamide-based conjugates *cis*-**8** and *cis*-**9**, as promising therapeutic agents acting on mitoK_v1.3 for targeting tumor cells. These conjugates demonstrated a significant ability to disrupt mitochondrial function by inducing rapid depolarization of the mitochondrial inner membrane and increasing ROS production, though to a much lesser extent than psoralen-based conjugates PAPTP and PCARBTP. Importantly, *cis*-**8** and *cis*-**9** exhibited selective cytotoxicity towards tumor cells across various models, including murine melanoma (B16F10), human pancreatic cancer (COLO 357), and pancreatic-derived organoids, while sparing non-tumor cells such as hTERT-RPE1. This selective toxicity was closely linked to their ability to inhibit K_v1.3 channels, as evidenced by the reduced sensitivity of K_v1.3-silenced B16F10 cells. The induction of apoptosis by *cis*-**8** and *cis*-**9**, as shown by caspase-3/7 activation in both 2D and 3D cell cultures, further validates their mechanism of action and potential efficacy in tumor therapy. The more pronounced effects observed in 3D spheroids and organoids suggest that these compounds can effectively penetrate and act within more complex tumor environments. Overall, our findings support the continued development of *cis*-**8** and *cis*-**9** as potent mitoK_v1.3-targeted anticancer agents. Future studies should focus on optimizing their pharmacokinetic properties, assessing their *in vivo* efficacy and safety, and exploring their potential synergistic effects with other therapeutic modalities.

Ethics approval statement and consent to participate

It is not applicable for the article.

Funding statement

This research was supported by ARIS project P1–0208, ARIS J7–4635, HE CutCancer project (101079113) and ARIS P1–0245. I.S is grateful to AIRC (IG Grant 20286) and WWCR (grant number 22–0348). The work has also received funding from the Max-Planck Society and from the European Union through Horizon 2020 research and innovation programme under the Marie Skłodowska-Curie grant agreement No. 813834-PHIONIC-H2020-MSCA-ITN-2018.

Permission to reproduce material from other sources

No. It is not applicable for the article.

CRediT authorship contribution statement

Ildiko Szabo: Writing – original draft, Supervision, Resources, Methodology, Investigation, Conceptualization. **Katja Kološa:** Writing – original draft, Visualization, Formal analysis, Data curation, Conceptualization. **Heike Wulff:** Writing – original draft, Validation, Supervision, Methodology, Investigation, Conceptualization. **Alja Štern:** Formal analysis, Data curation, Conceptualization. **Jesenko Tina:** Formal analysis, Data curation, Conceptualization. **Maja Čemažar:** Writing – original draft, Supervision, Project administration, Methodology, Funding acquisition, Conceptualization. **Daniela Secci:** Formal analysis, Data curation. **Andrej Emanuel Cotman:** Supervision. **Gayathri Viswanathan:** Formal analysis, Data curation. **Tihomir Tomašič:** Writing – original draft, Supervision, Methodology, Conceptualization. **Vanessa Checchetto:** Formal analysis, Data curation,

Conceptualization. **Peterlin Masic Lucija:** Writing – review & editing, Writing – original draft, Supervision, Resources, Methodology, Funding acquisition, Conceptualization. **Tina Kosjek:** Writing – original draft, Visualization, Methodology, Formal analysis, Data curation, Conceptualization. **Joshua A. Nasburg:** Formal analysis, Data curation. **Bojana Žegura:** Writing – original draft, Validation, Supervision, Resources, Project administration, Methodology, Conceptualization. **Hai M. Nguyen:** Formal analysis, Data curation. **Boštjan Markelc:** Writing – original draft, Visualization, Methodology, Investigation, Formal analysis, Data curation, Conceptualization. **Xiaoyi Shi:** Formal analysis, Data curation. **Ivan Džajić:** Formal analysis, Data curation. **Pardo Luis. A.:** Writing – review & editing, Writing – original draft, Visualization, Validation, Supervision, Resources, Methodology, Investigation, Funding acquisition, Formal analysis, Data curation, Conceptualization. **Maša Omerzel:** Visualization, Formal analysis, Data curation, Conceptualization. **Špela Gubič:** Writing – original draft, Visualization, Investigation, Formal analysis, Data curation, Conceptualization. **Tim Božič:** Formal analysis, Data curation, Conceptualization. **Marzia Fois:** Formal analysis.

Declaration of Competing Interest

The authors declare that they have no known competing financial interests or personal relationships that could have appeared to influence the work reported in this paper.

Appendix A. Supporting information

Supplementary data associated with this article can be found in the online version at doi:10.1016/j.biopha.2026.118996.

Data availability

Data will be made available on request.

References

[1] G. Yellen, The Voltage-Gated Potassium Channels and Their Relatives, Nature 419 (6902) (2002) 35–42, https://doi.org/10.1038/nature00978.

[2] Q. Kuang, P. Purhonen, H. Hebert, Structure of Potassium Channels, Cell. Mol. Life Sci. CMLS 72 (19) (2015) 3677–3693, https://doi.org/10.1007/s00018-015-1948-5.

[3] I. Szabò, J. Bock, A. Jekle, M. Soddemann, C. Adams, F. Lang, M. Zoratti, E. Gulbins, A Novel Potassium Channel in Lymphocyte Mitochondria, J. Biol. Chem. 280 (13) (2005) 12790–12798, https://doi.org/10.1074/jbc.M413548200.

[4] S.H. Jang, J.K. Byun, W.-I. Jeon, S.Y. Choi, J. Park, B.H. Lee, J.E. Yang, J.B. Park, S. M. O'Grady, D.-Y. Kim, P.D. Ryu, S.-W. Joo, S.Y. Lee, Nuclear Localization and Functional Characteristics of Voltage-Gated Potassium Channel Kv1.3, J. Biol. Chem. 290 (20) (2015) 12547–12557, https://doi.org/10.1074/jbc.M114.561324.

[5] J. Zhu, J. Yan, W.B. Thornhill, The Kv1.3 Potassium Channel Is Localized to the Cis-Golgi and Kv1.6 Is Localized to the Endoplasmic Reticulum in Rat Astrocytes, FEBS J. 281 (15) (2014) 3433–3445, https://doi.org/10.1111/febs.12871.

[6] E. Prosdocimi, V. Checchetto, L. Leanza, Targeting the Mitochondrial Potassium Channel Kv1.3 to Kill Cancer Cells: Drugs, Strategies, and New Perspectives, SLAS Discov. Adv. Life Sci. R. D. 24 (9) (2019) 882–892, https://doi.org/10.1177/2472555219864894.

[7] J. Capera, M. Navarro-Pérez, A.S. Moen, I. Szabó, A. Felipe, The Mitochondrial Routing of the Kv1.3 Channel, Front. Oncol. 12 (2022) 865686, https://doi.org/10.3389/fonc.2022.865686.

[8] I. Szabó, J. Bock, H. Grassmé, M. Soddemann, B. Wilker, F. Lang, M. Zoratti, E. Gulbins, Mitochondrial Potassium Channel Kv1.3 Mediates Bax-Induced Apoptosis in Lymphocytes, Proc. Natl. Acad. Sci. U. S. A. 105 (39) (2008) 14861–14866, https://doi.org/10.1073/pnas.0804236105.

[9] E. Prosdocimi, V. Carpanese, L.M. Todesca, T. Varanita, M. Bachmann, M. Festa, D. Bonesso, M. Perez-Verdaguer, A. Carrer, A. Velle, R. Peruzzo, S. Muccioli, D. Doni, L. Leanza, P. Costantini, F. Stein, M. Rettel, A. Felipe, M.J. Edwards, E. Gulbins, L. Cendron, C. Romualdi, V. Checchetto, I. Szabo, Bioid-Based Intact Cell Interactome of the Kv1.3 Potassium Channel Identifies a Kv1.3-Stat3-P53 Cellular Signaling Pathway, Sci. Adv. (2024).

[10] J. Bielanska, J. Hernández-Losa, M. Pérez-Verdaguer, T. Moline, R. Somoza, Y. Ramón, S. Cajal, E. Condom, J.C. Ferreres, A. Felipe, Voltage-Dependent Potassium Channels Kv1.3 and Kv1.5 in Human Cancer, Curr. Cancer Drug Targets 9 (8) (2009) 904–914, https://doi.org/10.2174/156800909790192400.

[11] A. Teisseyre, A. Palko-Labuz, K. Sroda-Pomianek, K. Michalak, Voltage-gated potassium channel Kv1.3 as a target in therapy of cancer, Front Oncol. 9 (2019) 933.

[12] A. Teisseyre, A. Palko-Labuz, K. Sroda-Pomianek, K. Michalak, Voltage-gated potassium channel Kv1.3 as a target in therapy of cancer. Ion Channels in Cancer, IntechOpen, 2020.

[13] A. Wrzosek, B. Augustynek, M. Żochowska, A. Szewczyk, Mitochondrial potassium channels as druggable targets, Biomolecules 10 (8) (2020) 1200.

[14] N. Comes, J. Bielanska, A. Vallejo-Gracia, A. Serrano-Albarrás, L. Marruecos, D. Gómez, C. Soler, E. Condom, S. Ramón y Cajal, J. Hernández-Losa, J.C. Ferreres, A. Felipe, The Voltage-Dependent K+ Channels Kv1.3 and Kv1.5 in Human Cancer, Front. Physiol. 4 (2013) 283, https://doi.org/10.3389/fphys.2013.00283.

[15] N. Comes, A. Serrano-Albarrás, J. Capera, C. Serrano-Novillo, E. Condom, S. Ramón Y Cajal, J.C. Ferreres, A. Felipe, Involvement of Potassium Channels in the Progression of Cancer to a More Malignant Phenotype, Biochim. Biophys. Acta 1848 (10 Pt B) (2015) 2477–2492, https://doi.org/10.1016/j.bbamem.2014.12.008.

[16] M. Uhlén, L. Fagerberg, B.M. Hallström, et al., KCNA3 protein expression in human cell lines, Hum. Protein Atlas [Internet] (2025) cited 2025 Dec 23].

[17] M. Bachmann, G. Pontarin, I. Szabo, The Contribution of Mitochondrial Ion Channels to Cancer Development and Progression, Cell. Physiol. Biochem. Int. J. Exp. Cell. Physiol. Biochem. Pharm. 53 (2019) 63–78, https://doi.org/10.33594/000000198.

[18] A. Teisseyre, J. Gąsiorowska, K. Michalak, Voltage-Gated Ptassium Channels Kv1.3 - Potentially New Molecular Target in Cancer Diagnostics and Therapy, Adv. Clin. Exp. Med. 24 (2015) 517–524, https://doi.org/10.17219/acem/22339.

[19] V. Checchetto, E. Prosdocimi, L. Leanza, Mitochondrial Kv1.3: A New Target in Cancer Biology? Cell. Physiol. Biochem. Int. J. Exp. Cell. Physiol. Biochem. Pharm. 53 (S1) (2019) 52–62, https://doi.org/10.33594/000000195.

[20] A. Teisseyre, A. Palko-Labuz, K. Sroda-Pomianek, K. Michalak, Voltage-Gated Potassium Channel Kv1.3 as a Target in Therapy of Cancer, Front. Oncol. 9 (2019) 933, https://doi.org/10.3389/fonc.2019.00933.

[21] L. Leanza, M. Romio, K.A. Becker, M. Azzolini, L. Trentin, A. Managò, E. Venturini, A. Zaccagnino, A. Mattarei, L. Carraretto, A. Urbani, S. Kadow, L. Biasutto, V. Martini, F. Severin, R. Peruzzo, V. Trimarco, J.-H. Egberts, C. Hauser, A. Visentin, G. Semenzato, H. Kalthoff, M. Zoratti, E. Gulbins, C. Paradisi, I. Szabo, Direct Pharmacological Targeting of a Mitochondrial Ion Channel Selectively Kills Tumor Cells In Vivo, Cancer Cell 31 (4) (2017) 516–531.e10, https://doi.org/10.1016/j.ccell.2017.03.003.

[22] C. Nguyen, S. Pandey, Exploiting Mitochondrial Vulnerabilities to Trigger Apoptosis Selectively in Cancer Cells, Cancers 11 (7) (2019) E916, https://doi.org/10.3390/cancers11070916.

[23] I. Szabo, M. Zoratti, L. Biasutto, Targeting Mitochondrial Ion Channels for Cancer Therapy, Redox Biol. 42 (2021) 101846, https://doi.org/10.1016/j.redox.2020.101846.

[24] G. Battogtokh, Y.-Y. Cho, J.Y. Lee, H.S. Lee, H.C. Kang, Mitochondrial-Targeting Anticancer Agent Conjugates and Nanocarrier Systems for Cancer Treatment, Front. Pharm. 9 (2018) 922, https://doi.org/10.3389/fphar.2018.00922.

[25] S. Parrasia, A. Mattarei, A. Furlan, M. Zoratti, L. Biasutto, Small-Molecule Modulators of Mitochondrial Channels as Chemotherapeutic Agents, Cell. Physiol. Biochem. Int. J. Exp. Cell. Physiol. Biochem. Pharm. 53 (S1) (2019) 11–43, https://doi.org/10.33594/000000192.

[26] A. Schmitz, A. Sankaranarayanan, P. Azam, K. Schmidt-Lassen, D. Homerick, W. Hänsel, H. Wulff, Design of PAP-1, a Selective Small Molecule Kv1.3 Blocker, for the Suppression of Effector Memory T Cells in Autoimmune Diseases, Mol. Pharm. 68 (5) (2005) 1254–1270, https://doi.org/10.1124/mol.105.015669.

[27] A. Mattarei, M. Romio, A. Managò, M. Zoratti, C. Paradisi, I. Szabò, L. Leanza, L. Biasutto, Novel Mitochondria-Targeted Furocoumarin Derivatives as Possible Anti-Cancer Agents, Front. Oncol. 8 (2018) 122, https://doi.org/10.3389/fonc.2018.00122.

[28] L. Leanza, B. Henry, N. Sassi, M. Zoratti, K.G. Chandy, E. Gulbins, I. Szabò, Inhibitors of Mitochondrial Kv1.3 Channels Induce Bax/Bak-Independent Death of Cancer Cells, EMBO Mol. Med. 4 (7) (2012) 577–593, https://doi.org/10.1002/emmm.201200235.

[29] W. Li, G.C. Wilson, M. Bachmann, J. Wang, A. Mattarei, C. Paradisi, M.J. Edwards, I. Szabo, E. Gulbins, S.A. Ahmad, S.H. Patel, Inhibition of a Mitochondrial Potassium Channel in Combination with Gemcitabine and Abraxane Drastically Reduces Pancreatic Ductal Adenocarcinoma in an Immunocompetent Orthotopic Murine Model, Cancers 14 (11) (2022) 2618, https://doi.org/10.3390/cancers14112618.

[30] F. Severin, A. Urbani, T. Varanita, M. Bachmann, M. Azzolini, V. Martini, M. Pizzi, A.P.D. Tos, F. Frezzato, A. Mattarei, P. Ghia, M.T.S. Bertilaccio, E. Gulbins, C. Paradisi, M. Zoratti, G.C. Semenzato, L. Leanza, L. Trentin, I. Szabò, Pharmacological Modulation of Kv1.3 Potassium Channel Selectively Triggers Pathological B Lymphocyte Apoptosis in Vivo in a Genetic CLL Model, J. Exp. Clin. Cancer Res. 41 (1) (2022) 64, https://doi.org/10.1186/s13046-022-02249-w.

[31] *PAP-1 Datasheet.* ⟨https://www.selleckchem.com/datasheet/pap-1-E037801-DataSheet.html⟩ (accessed 2022-06-13).

[32] W.A. Schmalhofer, J. Bao, O.B. McManus, B. Green, M. Matyskiela, D. Wunderler, R.M. Bugianesi, J.P. Felix, M. Hanner, A.-R. Linde-Arias, C.G. Ponte, L. Velasco, G. Koo, M.J. Staruch, S. Miao, W.H. Parsons, K. Rupprecht, R.S. Slaughter, G. J. Kaczorowski, M.L. Garcia, Identification of a New Class of Inhibitors of the Voltage-Gated Potassium Channel, Kv1.3, with Immunosuppressant Properties, Biochemistry 41 (24) (2002) 7781–7794, https://doi.org/10.1021/bi025722c.

[33] Š. Gubič, A. Montalbano, C. Sala, A. Becchetti, L.A. Hendrickx, K.M. Van Theemsche, E.L. Pinheiro-Junior, G.C. Altadonna, S. Peigneur, J. Ilaš, A.J. Labro, L.

A. Pardo, J. Tytgat, T. Tomašič, A. Arcangeli, L. Peterlin Mašič, Immunosuppressive Effects of New Thiophene-Based KV1.3 Inhibitors, Eur. J. Med. Chem. 259 (2023) 115561, https://doi.org/10.1016/j.ejmech.2023.115561.

[34] A. Zaccagnino, A. Managò, L. Leanza, A. Gontarewitz, B. Linder, M. Azzolini, L. Biasutto, M. Zoratti, R. Peruzzo, K. Legler, A. Trauzold, H. Kalthoff, I. Szabo, Tumor-Reducing Effect of the Clinically Used Drug Clofazimine in a SCID Mouse Model of Pancreatic Ductal Adenocarcinoma, Oncotarget 8 (24) (2017) 38276–38293, https://doi.org/10.18632/oncotarget.11299.

[35] J. Zielonka, J. Joseph, A. Sikora, M. Hardy, O. Ouari, J. Vasquez-Vivar, G. Cheng, M. Lopez, B. Kalyanaraman, Mitochondria-Targeted Triphenylphosphonium-Based Compounds: Syntheses, Mechanisms of Action, and Therapeutic and Diagnostic Applications, Chem. Rev. 117 (15) (2017) 10043–10120, https://doi.org/10.1021/acs.chemrev.7b00042.

[36] M.P. Murphy, Selective Targeting of Bioactive Compounds to Mitochondria, Trends Biotechnol. 15 (8) (1997) 326–330, https://doi.org/10.1016/S0167-7799(97)01068-8.

[37] E.A. Liberman, V.P. Topaly, L.M. Tsofina, A.A. Jasaitis, V.P. Skulachev, Mechanism of Coupling of Oxidative Phosphorylation and the Membrane Potential of Mitochondria, Nature 222 (5198) (1969) 1076–1078, https://doi.org/10.1038/2221076a0.

[38] H. Wulff, P.A. Calabresi, R. Allie, S. Yun, M. Pennington, C. Beeton, K.G. Chandy, The Voltage-Gated Kv1.3 K(+) Channel in Effector Memory T Cells as New Target for MS, J. Clin. Invest 111 (11) (2003) 1703–1713, https://doi.org/10.1172/JCI16921.

[39] R. Peruzzo, A. Mattarei, M. Azzolini, K.A. Becker-Flegler, M. Romio, G. Rigoni, A. Carrer, L. Biasutto, S. Parrasia, S. Kadow, A. Managò, A. Urbani, A. Rossa, G. Semenzato, M.E. Soriano, L. Trentin, S. Ahmad, M. Edwards, E. Gulbins, C. Paradisi, M. Zoratti, L. Leanza, I. Szabò, Insight into the Mechanism of Cytotoxicity of Membrane-Permeant Psoralenic Kv1.3 Channel Inhibitors by Chemical Dissection of a Novel Member of the Family, Redox Biol. 37 (2020) 101705, https://doi.org/10.1016/j.redox.2020.101705.

[40] A. Mattarei, L. Biasutto, E. Marotta, U. De Marchi, N. Sassi, S. Garbisa, M. Zoratti, C. Paradisi, A. mitochondriotropic derivative of quercetin: a strategy to increase the effectiveness of polyphenols, ChemBioChem 9 (2008) 2633–2642.

[41] V. Checchetto, L. Leanza, D. De Stefani, R. Rizzuto, E. Gulbins, I. Szabo, Mitochondrial K+ Channels and Their Implications for Disease Mechanisms, Pharmacol. Ther. 227 (2021) 107874.

[42] K. Banki, E. Hutter, N.J. Gonchoroff, A. Perl, Elevation of Mitochondrial Transmembrane Potential and Reactive Oxygen Intermediate Levels Are Early Events and Occur Independently from Activation of Caspases in Fas Signaling, J. Immunol. Baltim. Md 1950 162 (3) (1999) 1466–1479.

[43] C. Giovannini, P. Matarrese, B. Scazzocchio, M. Sanchez, R. Masella, W. Malorni, Mitochondria Hyperpolarization Is an Early Event in Oxidized Low-Density Lipoprotein-Induced Apoptosis in Caco-2 Intestinal Cells, FEBS Lett. 523 (1–3) (2002) 200–206, https://doi.org/10.1016/s0014-5793(02)02972-1.

[44] P. Selvakumar, A.I. Fernández-Mariño, N. Khanra, C. He, A.J. Paquette, B. Wang, R. Huang, V.V. Smider, W.J. Rice, K.J. Swartz, J.R. Meyerson, Structures of the T Cell Potassium Channel Kv1.3 with Immunoglobulin Modulators, Nat. Commun. 13 (1) (2022) 3854, https://doi.org/10.1038/s41467-022-31285-5.

[45] J.C. Shelley, A. Cholleti, L.L. Frye, J.R. Greenwood, M.R. Timlin, M. Uchimaya, Epik: A Software Program for pKaprediction and Protonation State Generation for Drug-like Molecules, J. Comput. Aided Mol. Des. 21 (12) (2007) 681–691, https://doi.org/10.1007/s10822-007-9133-z.

[46] S. Grissmer, A.N. Nguyen, J. Aiyar, D.C. Hanson, R.J. Mather, G.A. Gutman, M. J. Karmilowicz, D.D. Auperin, K.G. Chandy, Pharmacological Characterization of Five Cloned Voltage-Gated K+ Channels, Types Kv1.1, 1.2, 1.3, 1.5, and 3.1, Stably Expressed in Mammalian Cell Lines, Mol. Pharm. 45 (6) (1994) 1227–1234.

[47] S.F. Boj, C.-I. Hwang, L.A. Baker, I.I.C. Chio, D.D. Engle, V. Corbo, M. Jager, M. Ponz-Sarvise, H. Tiriac, M.S. Spector, A. Gracanin, T. Oni, K.H. Yu, R. van Boxtel, M. Huch, K.D. Rivera, J.P. Wilson, M.E. Feigin, D. Öhlund, A. Handly-Santana, C.M. Ardito-Abraham, M. Ludwig, E. Elyada, B. Alagesan, G. Biffi, G. N. Yordanov, B. Delcuze, B. Creighton, K. Wright, Y. Park, F.H.M. Morsink, I. Q. Molenaar, I.H. Borel Rinkes, E. Cuppen, Y. Hao, Y. Jin, I.J. Nijman, C. Iacobuzio-Donahue, S.D. Leach, D.J. Pappin, M. Hammell, D.S. Klimstra, O. Basturk, R. H. Hruban, G.J. Offerhaus, R.G.J. Vries, H. Clevers, D.A. Tuveson, Organoid Models of Human and Mouse Ductal Pancreatic Cancer, Cell 160 (1–2) (2015) 324–338, https://doi.org/10.1016/j.cell.2014.12.021.

[48] C. Vianello, F. Dal Bello, S.H. Shin, S. Schiavon, C. Bean, A.P. Magalhães Rebelo, T. Knedlík, E.N. Esfahani, V. Costiniti, R.S. Lacruz, G. Covello, F. Munari, T. Scolaro, A. Viola, E. Rampazzo, L. Persano, S. Zumerle, L. Scorrano, A. Gianelle, M. Giacomello, High-Throughput Microscopy Analysis of Mitochondrial Membrane Potential in 2D and 3D Models, Cells 12 (7) (2023) 1089, https://doi.org/10.3390/cells12071089.

[49] B. Žegura, M. Filipič, Application of In Vitro Comet Assay for Genotoxicity Testing, in: Z. Yan, G.W. Caldwell (Eds.), Optimization in Drug Discovery: In Vitro Methods, Humana Press, Totowa, NJ, 2004, pp. 301–313, https://doi.org/10.1385/1-59259-800-5:301.

[50] OECD. Test No. 487: In Vitro Mammalian Cell Micronucleus Test, 2023. ⟨https://www.oecd-ilibrary.org/content/publication/9789264264861-en⟩.

[51] A. Štraser, M. Filipič, B. Žegura, Genotoxic Effects of the Cyanobacterial Hepatotoxin Cylindrospermopsin in the HepG2 Cell Line, Arch. Toxicol. 85 (12) (2011) 1617–1626, https://doi.org/10.1007/s00204-011-0716-z.

[52] K. Hercog, S. Maisanaba, M. Filipič, M. Sollner-Dolenc, L. Kač, B. Žegura, Genotoxic Activity of Bisphenol A and Its Analogues Bisphenol S, Bisphenol F and Bisphenol AF and Their Mixtures in Human Hepatocellular Carcinoma (HepG2) Cells, Sci. Total Environ. 687 (2019) 267–276, https://doi.org/10.1016/j.scitotenv.2019.05.486.

[53] M. Sendra, M. Štampar, K. Fras, B. Novoa, A. Figueras, B. Žegura, Adverse (Geno) Toxic Effects of Bisphenol A and Its Analogues in Hepatic 3D Cell Model, Environ. Int. 171 (2023) 107721, https://doi.org/10.1016/j.envint.2022.107721.